

# Northumbria Research Link

Citation: Klages, Johann P., Salzmänn, Ulrich, Bickert, Torsten, Hillenbrand, Claus-Dieter, Gohl, Karsten, Kuhn, Gerhard, Bohaty, Steven M., Titschack, Jürgen, Müller, Juliane, Frederichs, Thomas, Bauersachs, Thorsten, Ehrmann, Werner, van de Flierdt, Tina, Pereira, Patric Simões, Larter, Robert D., Lohmann, Gerrit, Niezgodzki, Igor, Uenzelmann-Neben, Gabriele, Zundel, Maximilian, Spiegel, Cornelia, Mark, Chris, Chew, David, Francis, Jane E., Nehrke, Gernot, Schwarz, Florian, Smith, James A., Freudenthal, Tim, Esper, Oliver, Pälke, Heiko, Ronge, Thomas A., Dziadek, Ricarda, Afanasyeva, V., Arndt, J. E., Ebermann, B., Gebhardt, C., Hochmuth, K., Küssner, K., Najman, Y., Riefstahl, F. and Scheinert, M. (2020) Temperate rainforests near the South Pole during peak Cretaceous warmth. *Nature*, 580 (7801). pp. 81-86. ISSN 1476-4687

Published by: Nature Publishing

URL: <https://doi.org/10.1038/s41586-020-2148-5> <<https://doi.org/10.1038/s41586-020-2148-5>>

This version was downloaded from Northumbria Research Link:  
<http://nrl.northumbria.ac.uk/id/eprint/42650/>

Northumbria University has developed Northumbria Research Link (NRL) to enable users to access the University's research output. Copyright © and moral rights for items on NRL are retained by the individual author(s) and/or other copyright owners. Single copies of full items can be reproduced, displayed or performed, and given to third parties in any format or medium for personal research or study, educational, or not-for-profit purposes without prior permission or charge, provided the authors, title and full bibliographic details are given, as well as a hyperlink and/or URL to the original metadata page. The content must not be changed in any way. Full items must not be sold commercially in any format or medium without formal permission of the copyright holder. The full policy is available online: <http://nrl.northumbria.ac.uk/policies.html>

This document may differ from the final, published version of the research and has been made available online in accordance with publisher policies. To read and/or cite from the published version of the research, please visit the publisher's website (a subscription may be required.)



**Northumbria  
University**  
NEWCASTLE



University**Library**

1 Temperate rainforests near the South Pole during peak  
2 Cretaceous warmth

3

4 Klages, J.P.<sup>1\*</sup>, Salzmann, U.<sup>2</sup>, Bickert, T.<sup>3</sup>, Hillenbrand, C.-D.<sup>4</sup>, Gohl, K.<sup>1</sup>, Kuhn, G.<sup>1</sup>,  
5 Bohaty, S.<sup>5</sup>, Titschack, J.<sup>3,6</sup>, Müller, J.<sup>1,7</sup>, Frederichs, T.<sup>7</sup>, Bauersachs, T.<sup>8</sup>, Ehrmann,  
6 W.<sup>9</sup>, van de Fliedrt, T.<sup>10</sup>, Simões Pereira, P.<sup>10+</sup>, Larter, R.D.<sup>4</sup>, Lohmann, G.<sup>1,3,11</sup>,  
7 Niezgodzki, I.<sup>1,12</sup>, Uenzelmann-Neben, G.<sup>1</sup>, Zundel, M.<sup>7</sup>, Spiegel, C.<sup>7</sup>, Mark, C.<sup>13++</sup>,  
8 Chew, D.<sup>13</sup>, Francis, J.E.<sup>4</sup>, Nehrke, G.<sup>1</sup>, Schwarz, F.<sup>2</sup>, Smith, J.A.<sup>4</sup>, Freudenthal, T.<sup>3</sup>,  
9 Esper, O.<sup>1</sup>, Pälike, H.<sup>3</sup>, Ronge, T.<sup>1</sup>, Dziadek, R.<sup>1</sup>, and the Science Team of  
10 Expedition PS104<sup>‡</sup>

11

12 <sup>1</sup> Alfred-Wegener-Institut Helmholtz-Zentrum für Polar- und Meeresforschung, Bremerhaven, Germany

13 <sup>2</sup> Northumbria University, Department of Geography and Environmental Sciences, Newcastle upon Tyne, United  
14 Kingdom

15 <sup>3</sup> MARUM – Center for Marine Environmental Sciences, Bremen, Germany

16 <sup>4</sup> British Antarctic Survey, Cambridge, United Kingdom

17 <sup>5</sup> School of Ocean and Earth Science, University of Southampton, Southampton, United Kingdom

18 <sup>6</sup> Senckenberg am Meer (SAM), Marine Research Department, Wilhelmshaven, Germany

19 <sup>7</sup> University of Bremen, Faculty of Geosciences, Bremen, Germany

20 <sup>8</sup> Christian-Albrechts-University, Institute of Geoscience, Kiel, Germany

21 <sup>9</sup> University of Leipzig, Institute for Geophysics and Geology, Leipzig, Germany

22 <sup>10</sup> Imperial College London, Department of Earth Science & Engineering, London, United Kingdom

23 <sup>11</sup> University of Bremen, Environmental Physics, Bremen, Germany

24 <sup>12</sup> ING PAN – Institute of Geological Sciences, Polish Academy of Sciences, Biogeosystem Modelling Laboratory,  
25 Kraków, Poland

26 <sup>13</sup> Department of Geology, Trinity College Dublin, Dublin, Ireland

27 <sup>\*</sup> now at: University of Gothenburg, Department of Marine Sciences, Gothenburg, Sweden

28 <sup>++</sup> now at: School of Earth Sciences, University College Dublin, Dublin, Ireland

29 <sup>‡</sup> A full list of authors and their affiliations appears at the end of the paper

30 <sup>\*</sup> Corresponding author: Johann.Klages@awi.de

31 **The mid-Cretaceous was one of the warmest intervals of the past 140 million years**  
32 **(Myr)<sup>1–5</sup> driven by atmospheric CO<sub>2</sub> levels around 1000 ppmv<sup>6</sup>. In the near absence of**  
33 **proximal geological records from south of the Antarctic Circle, it remains disputed**  
34 **whether polar ice could exist under such environmental conditions. Here we present**  
35 **results from a unique sedimentary sequence recovered from the West Antarctic shelf.**  
36 **This by far southernmost Cretaceous record contains an intact ~3 m-long network of**  
37 ***in-situ* fossil roots. The roots are embedded in a mudstone matrix bearing diverse**  
38 **pollen and spores, indicative of a temperate lowland rainforest environment at a**  
39 **palaeolatitude of ~82°S during the Turonian–Santonian (92–83 Myr). A climate model**  
40 **simulation shows that the reconstructed temperate climate at this high latitude**  
41 **requires a combination of both atmospheric CO<sub>2</sub> contents of 1120–1680 ppmv and a**  
42 **vegetated land surface without major Antarctic glaciation, highlighting the important**  
43 **cooling effect exerted by ice albedo in high-CO<sub>2</sub> climate worlds.**

44

45 The Cretaceous Period (144–66 Myr) hosted some of the warmest intervals in Earth's  
46 history<sup>1–3</sup>, particularly during its Turonian to Santonian stages (93.9–83.6 Myr)<sup>4,5</sup>. At that time,  
47 atmospheric carbon dioxide (CO<sub>2</sub>) concentrations were reconstructed to be around 1000  
48 ppmv<sup>6</sup>, and average annual low latitude sea surface temperatures probably reached ~35°C<sup>4</sup>,  
49 with only a minor bi-hemispheric temperature gradient extending poleward from palaeo-  
50 latitudes between 50–60°N (refs. 7–9). Only small to medium-sized ice sheets may have  
51 existed<sup>10,11</sup> and global sea level was up to 170 m higher than at present<sup>11,12</sup>.

52 Records documenting the Antarctic terrestrial environment during mid-Cretaceous warmth  
53 are sparse<sup>5,13–17</sup> and particularly rare south of the palaeo-Antarctic Circle<sup>13,14</sup>. Such records,  
54 however, are critical to constrain state-of-the-art Late Cretaceous climate models<sup>5</sup> for  
55 predicting the magnitude of atmospheric CO<sub>2</sub> concentrations<sup>18</sup> and their effectiveness in  
56 inhibiting the build-up of major ice sheets<sup>19</sup>.

57 Here we reconstruct mid-Cretaceous terrestrial environmental conditions in West Antarctica  
58 by combining micro- and macropalaeontological, sedimentological, inorganic and organic  
59 geochemical, mineralogical, and palaeomagnetic data as well as X-ray computed  
60 tomography (CT) imagery obtained from drill cores recovered from a site within the Pine  
61 Island cross-shelf trough in the Amundsen Sea Embayment (ASE), West Antarctica (Fig. 1a).  
62 Site PS104\_20-2 (73.57°S, 107.09°W; 946 m water depth) was drilled during RV *Polarstern*  
63 expedition PS104 in 2017 (ref. 22). The Pine Island Trough extends from the modern fronts  
64 of Pine Island and Thwaites glaciers, and was eroded into the ASE shelf during repeated  
65 advances of a West Antarctic Ice Sheet (WAIS) palaeo-ice stream throughout Miocene–  
66 Pleistocene epochs<sup>23–25</sup>. On the inner–middle continental shelf, glacial erosion combined with  
67 tectonic uplift<sup>24</sup> exposed seaward-dipping sedimentary strata of postulated Cretaceous to  
68 Miocene age near the seafloor<sup>26</sup> (Fig. 1b). Widespread till cover on the shelf previously  
69 prevented sampling of these strata using conventional coring techniques<sup>26</sup>. Deployment of  
70 the remotely operated seafloor drill rig *MARUM-MeBo70* (ref. 27) enabled drilling to 30.7  
71 metres below sea floor (mbsf) into the seabed and recover the dipping strata<sup>22</sup> (Figs. 1, 2).

72

### 73 **Lithology and stratigraphy**

74 Beneath a few meters of glacimarine and reworked glacial sediments, *MARUM-MeBo70*  
75 penetrated occasionally stratified but microfossil-barren ca. 17 to 24 m-thick quartzitic  
76 sandstone with uranium/lead (U/Pb) dates on apatite and zircon grains (see Methods)  
77 constraining its maximum depositional age to ~40 Myr in the late Eocene (Extended Data  
78 Fig. 1). Cores 9R and 10R recovered strata from 26.3 mbsf to the base of the hole. At ca.  
79 26.8 mbsf, a prominent 5 cm thin layer of indurated lignite fragments separates the overlying  
80 sandstone unit from a ≥3 m-thick palynomorph-rich, laminated to stratified carbonaceous  
81 mudstone below. This mudstone contains an intact and continuous network of fossil plant  
82 roots that reaches down to at least ~30 mbsf (Fig. 2; Supplementary Video 1).  
83 Based on New Zealand's biostratigraphic ranges<sup>28</sup>, the presence of the pollen taxon  
84 *Phyllocladites mawsonii* (Nearest Living Relative (NLR): *Lagarostrobos*, Huon Pine) and the

85 absence of both *Nothofagidites* (NLR: *Nothofagus*, Southern Beech) and *Forcipites*  
86 *sabulosus* within the carbonaceous mudstone indicate its deposition during the mid-  
87 Cretaceous (Turonian–Santonian; ~92–83 Myr, PM1a-subzone) (Extended Data Fig. 2;  
88 Extended Data Tables 1, 2). Abundant pollen of conifer trees (e.g. *Podocarpidites*,  
89 *Trichotomosulcites*), tree ferns (*Cyathidites*), and the presence of accessory taxa such as  
90 *Ruffordiaspora ludbrookiae* and *Tricolpites* spp. in our assemblage resemble the uppermost  
91 strata of the Turonian–Santonian Tupuangi Formation on Pitt Island, New Zealand, dated to  
92 92–89 Myr<sup>29,30</sup> (Extended Data Table 3). However, the regular occurrence of pollen of the  
93 family Proteaceae, including *Beauprea*-type pollen (e.g. *Peninsulapollis gillii*, *Beaupreadites*),  
94 which are absent from the Tupuangi Formation, suggest the ASE core to be slightly younger  
95 than 89 Myr. Recent molecular phylogenetic reconstructions indicate an early Antarctic-  
96 Southeastern Australian origin of *Beauprea* (~88 Myr ago), while the oldest palynological  
97 record of these angiosperm fossils on Antarctica and Australia date back to 81.4 Myr and  
98 83.8 Myr, respectively<sup>31</sup>.  
99 These biostratigraphic age estimates are consistent with palaeomagnetic data obtained from  
100 discrete sediment samples showing normal polarity, expected for deposition during the  
101 ‘Cretaceous Normal Polarity Superchron’ (C34n; 121–83 Myr; ref. 32) (see Methods). The  
102 layer of indurated lignite and the underlying carbonaceous mudstone show very similar  
103 pollen assemblages, which indicate a similar age and palaeoenvironment for both units (Fig.  
104 2; Extended Data Fig. 2).

105

#### 106 **Turonian–Santonian position of the record**

107 In order to assess the palaeoclimatic significance of this record, we determined the  
108 palaeogeographical position of site PS104\_20-2 at 90 Myr. Today, the site is located near  
109 the Pacific continental margin of West Antarctica about 250 km away from the modern  
110 boundary between continental and oceanic crust (Fig. 1). At the time of sediment deposition  
111 between 93 and 83 Myr, the continent of Zealandia started to rift and separate from West  
112 Antarctica<sup>33,34</sup>. We applied a relative plate reconstruction between Zealandia and West

113 Antarctica for the middle Cretaceous using the *GPlates* plate reconstruction tool<sup>35</sup> with up-to-  
114 date rotation parameters of the South Pacific realm<sup>33</sup>. This resulted in a 736-km great-circle  
115 distance (265 km North-South distance) between the drill site and the hitherto southernmost  
116 mid-Cretaceous terrestrial palaeoenvironmental record on Pitt Island on Chatham Rise, New  
117 Zealand<sup>14</sup>. The close fit reconstruction at 90 Myr indicates a wide rift zone between  
118 Zealandia and West Antarctica, just before initiation of the continental breakup<sup>26,33</sup>. In a  
119 previous study<sup>36</sup>, a 100-Myr mean palaeomagnetic pole position of 75.7°S and 135.9°W with  
120 a 95% confidence radius of 3.8° for Marie Byrd Land was determined from 19 rock sample  
121 sites. By accounting for the great-circle distance of 7.84° to our drill site and rotating points  
122 on the East Antarctic polar wander path<sup>36</sup> into the Marie Byrd Land reference frame, we  
123 derive a core site palaeolatitude of 81.9°S at 90 Myr. Its uncertainty is estimated to be not  
124 larger than the maximum 95% confidence radius of 5.9° of the respective part of the polar  
125 wander path<sup>36</sup>.

126

## 127 **Palaeoenvironment**

128 The indurated lignite layer as well as the laminated to stratified carbonaceous mudstone  
129 comprising the fossil plant roots in cores 10R and lower 9R at site PS104\_20-2 contain a  
130 highly diverse and entirely terrestrial palynomorph assemblage of more than 62 pollen and  
131 spore taxa (Fig. 2; Extended Data Figs. 2, 3; Extended Data Table 3). The absence of  
132 palynomorphs with different stratigraphic ranges or varying thermal maturity suggests that  
133 this purely terrestrial microfossil assemblage has not been reworked. The assemblage is  
134 dominated by pollen of the conifer tree families Podocarpaceae and Araucariaceae with  
135 abundant ferns, including the tree ferns *Cyathea*, documenting the initial stages of an Austral  
136 temperate rainforest (Fig. 2; Extended Data Fig. 2; Extended Data Table 2). The presence of  
137 the heterocyst glycolipids HG<sub>30</sub> triol and keto-diol (Extended Data Fig. 4; see Methods) also  
138 indicates that benthic cyanobacterial mats colonized fresh water bodies within this temperate  
139 rainforest, providing additional evidence for the development of a highly complex ecosystem  
140 in the ASE during the Turonian–Santonian. In combination with published palaeo-

141 topographic and palaeo-tectonic information<sup>24,26,33,34</sup>, the different taxa and their bioclimatic  
142 significance (see Methods) were combined and visualized to create Fig. 4. Members of the  
143 Proteaceae family presumably formed a flowering shrub understorey in the tall Late  
144 Cretaceous conifer rainforest of the ASE depicted in Fig. 4. The lignite layer is rich in spores  
145 of *Stereisporites antiquasporites* (NLR: Bryophyte, *Sphagnum*), which further suggest the  
146 temporary existence of a peat swamp in the diverse temperate lowland rainforest. This  
147 coincides with increasing *Peninsulapollis* pollen indicating increasing humidity<sup>37</sup> towards the  
148 record's top. Thin sections were carefully prepared from resin-impregnated core samples  
149 selected from cores 9R and 10R (see Methods) to characterize the fossil roots. Although cell  
150 structures were not sufficiently preserved for identification of the plant that grew the roots, the  
151 presence of parenchyma cells within the long and continuous roots likely identifies the  
152 network as vascular plant remains and thus confirms active plant growth at our site  
153 (Extended Data Fig. 5b–e). Further, the alignment of organic and clastic material within the  
154 laminated to stratified mudstone matrix (Extended Data Fig. 5a) suggests synchronous  
155 deposition of clastic particles and organic fragments.

156 Our environmental reconstruction is further supported by geochemical and biomarker data. In  
157 the mudstone between 29.80 and 27.03 mbsf and the indurated lignite interval (26.83–26.77  
158 mbsf), absent to very low halite and carbonate contents in the bulk sediment fraction  
159 combined with low total organic carbon/total nitrogen (TOC/TN) ratios and low ratios of  
160 higher land-plant-derived long-chain *n*-alkanes versus aquatic-sourced short-chain *n*-alkanes  
161 (TAR) point to swampy aquatic freshwater conditions (Fig. 2). This interpretation is supported  
162 by the identification of cells closely resembling aerenchyma (Extended Data Fig. 5d) usually  
163 being responsible for inter-cellular gas exchange under (semi-) permanent subaquatic  
164 growing conditions<sup>38</sup>. In mudstone samples taken from the core segment containing a  
165 particularly dense root network (27.03–26.83 mbsf), pollen and biomarkers indicate the  
166 establishment of terrestrial forest-type vegetation, whilst elevated pristane/*n*-C<sub>17</sub> and  
167 pristane/phytane ratios point to high abundance of terrigenous plant material (Extended Data  
168 Fig. 6; cf. refs. 39, 40), which is in line with the pollen-based interpretation of a terrestrial



169 rainforest environment. TOC/TN ratios >20 (Fig. 2) are consistent with this interpretation and  
170 indicate a primarily land plant source of organic matter<sup>41</sup> within this mudstone sequence.

171 The clay mineral assemblage in cores 9R and 10R is dominated by kaolinite (67–72%) and  
172 smectite (26–29%), both indicating chemical weathering activity under humid and (sub-)  
173 tropical climate conditions<sup>42</sup>. However, as this is not corroborated by our reconstructed  
174 climatic setting, we attribute kaolinite formation in the mudstone predominantly to the  
175 establishment of repeated swampy conditions, in which organic acids altered silicate  
176 minerals to kaolinite (= ‘Moorverwitterung’)<sup>43</sup>.

177 The lithological succession in cores 9R and 10R resemble the uppermost strata of the  
178 Turonian–Santonian Tupuangi Formation on Pitt Island, New Zealand<sup>29</sup>. The Pitt Island strata  
179 are characterized by interbedded carbonaceous siltstone, quartzo-feldspathic sandstone and  
180 lignite and/or peat layers. Similar to the sediment sequence described for the ASE, the  
181 Tupuangi Formation records a terrestrial, densely vegetated, and partly swampy fluviodeltaic  
182 environment<sup>14</sup>. Some 90 million years ago, the Tupuangi Formation was located in one of the  
183 rift basins developing before Zealandia separated from West Antarctica<sup>26,33</sup>, ~736 km away  
184 from Site PS104\_20-2 (Fig. 1). A diverse conifer forest surrounded by extensive river  
185 systems<sup>44,45</sup> appears to have covered both the Zealandian<sup>14</sup> and the West Antarctic  
186 conjugate continental margin during this early break-up phase.

187 The sharp lithological change from the fossil root-bearing mudstone with the thin layer of  
188 indurated lignite on top into the sandstone at 26.77 mbsf is marked by increased iron  
189 carbonate and halite contents and decreased TOC/TN and TAR ratios within the sandstone  
190 (Fig. 2), suggesting an estuarine and coastal environment. The U/Pb dates of max. ~40 Myr  
191 obtained from the sandstone (see Extended Data Fig. 1), which is coarse-grained at its base,  
192 indicate a significant hiatus between the mudstone (including the lignite) and the sandstone.  
193 Such a hiatus is consistent with neodymium (Nd) and strontium (Sr) isotope data, reflecting  
194 both a change in sediment provenance and a decrease in weathering intensity between the  
195 two lithologies (Fig. 2; see Methods). The time window of the hiatus coincides with slow  
196 erosion rates of a tectonically quiescent passive margin<sup>24,46</sup>, whereas Eocene/Oligocene

197 tectonic activity of the West Antarctic Rift System might have triggered renewed  
198 sedimentation of dominantly clastic material<sup>46,47</sup>.

199

## 200 **Palaeoclimate**

201 Multi-proxy evidence from our mid-Cretaceous sedimentary record reveals an environment at  
202 a palaeolatitude of ~82°S on the Antarctic continental margin that was characterised by a  
203 regional temperate climate warm enough to maintain a diverse temperate rainforest (Fig. 4)  
204 only ~900 km away from the palaeo-South Pole. Our palynomorph-based climate  
205 reconstruction based on the approach outlined in ref. 48 indicates mean annual temperatures  
206 of 13°C with precipitation around 1,120 mm/year. The temperature of the warmest summer  
207 month was around 18.5°C on average. Previous quantitative climate analyses from Antarctic  
208 records ~2,500 km further north resulted in late Coniacian–early Santonian mean annual  
209 temperatures of 15–21°C<sup>49,50</sup>, suggesting a shallow gradient to our site. NLR-based  
210 estimates of Late Cretaceous climate generally agree well with other temperature proxies<sup>49</sup>.  
211 However, the approach assumes similarity of climate requirements for fossil taxa and their  
212 NLRs. As with increasing age the phylogenetic relationships of a fossil taxon become more  
213 disparate, the assumption becomes less robust. We therefore applied an independent  
214 geochemical palaeothermometer based on heterocyst glycolipid distribution (HTI<sub>30</sub>)<sup>51</sup>, which  
215 corroborated our bioclimatic reconstructions by indicating austral summer lake or river-  
216 surface temperatures of ~20°C for the swampy rainforest (Extended Data Fig. 4; see  
217 Methods). Our record contains the hitherto southernmost evidence of Cretaceous terrestrial  
218 environmental conditions and reveals a mid-Cretaceous ‘greenhouse climate’ that was  
219 capable of maintaining temperate conditions much further south than previously  
220 documented<sup>14</sup>.

221

## 222 **Palaeoclimate modelling**

223 In light of extremely limited mid-Cretaceous CO<sub>2</sub> proxy data<sup>6</sup> and widely scattered existing  
224 data estimates<sup>5</sup> and in order to identify some of the pivotal driving mechanism of high-latitude

225 mid-Cretaceous environmental conditions reconstructed for our new record, we ran the  
226 global climate model COSMOS<sup>5</sup> in a coupled atmosphere–ocean configuration with fixed  
227 vegetation. We did so under present (Fig. 3a-c) and mid-Cretaceous configurations at 90 Myr  
228 (Fig. 3d-g) for 1x, 2x, 4x and 6x pre-industrial CO<sub>2</sub> levels of 280 ppm (280, 560, 1120 and  
229 1680 ppmv, respectively; see Methods). Although the model predicts a mid-Cretaceous  
230 climate in West Antarctica that is already warmer under pre-industrial CO<sub>2</sub> levels of 280 ppm  
231 (Fig. 3d), summer surface air and water temperatures of ~20°C at ~82°S can only be  
232 reproduced by forcing the climate with very high atmospheric CO<sub>2</sub> levels between 1120 and  
233 1680 ppmv (Fig. 3f, g). Our reconstructed mean annual temperature of 13°C, however, still  
234 remains significantly underestimated by the model (Fig. 3g).

235 We conclude that a temperate climate at such a high latitude with more than four months of  
236 complete polar night darkness requires a combination of both strongly elevated atmospheric  
237 CO<sub>2</sub> concentrations and dense surface vegetation that generates a low planetary albedo with  
238 an associated high radiant energy absorption and pronounced seasonality. This largely  
239 excludes the existence<sup>10</sup> of any substantial ice-sheet and sea-ice cover in and around  
240 Antarctica during the Turonian to Santonian stages of the Late Cretaceous epoch, likely  
241 additionally favoured by palaeo-geographic variations<sup>52</sup>. Conversely, the present Antarctic  
242 Ice Sheet and its associated climate feedbacks, such as the ice albedo, provide a stabilizing  
243 cooling effect in a future high-CO<sub>2</sub> world (Fig. 3a-c).

244 To further elaborate on the significance of additional forcing mechanisms, to discover the  
245 interdependency of surface vegetation and temperature sensitivity in more detail, and to  
246 explore the drivers of the late Cretaceous latitudinal gradient paradox visible in Fig. 3, future  
247 work will aim at running the model with various types of vegetation cover coupled with other  
248 drivers such as palaeo-geography<sup>52</sup> or changes in cloudiness<sup>53</sup>.

249 Our findings highlight the importance of including land–ice changes into long-term climate  
250 simulations in order to accurately estimate climate sensitivity on these extended time  
251 scales<sup>54</sup>. We provide new key data for constraining the response of polar terrestrial  
252 ecosystems to very high atmospheric CO<sub>2</sub> concentrations and for assessing the significance

253 of Antarctic ice sheet presence under high-CO<sub>2</sub> scenarios – essential for modelling both past  
254 and future climate change<sup>55</sup>.

255

- 256 1. Forster, A., Schouten, S., Baas, M. & Sinninghe Damsté, J. S. Mid-Cretaceous  
257 (Albian–Santonian) sea surface temperature record of the tropical Atlantic Ocean.  
258 *Geology* **35**, 919–922 (2007a).
- 259 2. Forster, A. et al. Tropical warming and intermittent cooling during the  
260 Cenomanian/Turonian Oceanic Anoxic Event (OAE 2): Sea surface temperature  
261 records from the equatorial Atlantic. *Paleoceanography* **22**, PA1219 (2007b).
- 262 3. Tarduno, J. A. et al. Evidence for Extreme Climatic Warmth from Late Cretaceous  
263 Arctic Vertebrates. *Science* **282**, 2241–2243 (1998).
- 264 4. O'Brien, C. L. et al. Cretaceous sea-surface temperature evolution: Constraints from  
265 TEX<sub>86</sub> and planktonic foraminiferal oxygen isotopes. *Earth-Sci. Rev.* **172**, 224–247  
266 (2017).
- 267 5. Niezgodzki, I. et al. Late Cretaceous climate simulations with different CO<sub>2</sub> levels and  
268 subarctic gateway configurations: A model-data comparison. *Paleoceanography* **32**,  
269 980–998 (2017).
- 270 6. Foster, G. L., Royer, D. L. & Lunt, D. J. Future climate forcing potentially without  
271 precedent in the last 420 million years. *Nat. Comm.* **8**, doi:10.1038/ncomms14845,  
272 (2017).
- 273 7. O'Connor, L. K. et al. Late Cretaceous Temperature Evolution of the Southern High  
274 Latitudes: A TEX<sub>86</sub> Perspective. *Paleoceanography and Paleoclimatology* **34**,  
275 doi:10.1029/2018PA003546 (2019).
- 276 8. Jenkyns, H. C., Forster, A., Schouten, S. & Sinninghe Damsté, S. High temperatures  
277 in the Late Cretaceous Arctic Ocean. *Nature* **432**, 888–892 (2004).
- 278 9. Ditchfield, P. W., Marshall, J. D. & Pirrie, D. High latitude palaeotemperature  
279 variation: New data from the Tithonian to Eocene of James Ross Island, Antarctica.  
280 *Palaeogeogr. Palaeoclimatol. Palaeoecol.* **107**, 79–101 (1994).

- 281 10. Bornemann, A. et al. Isotopic Evidence for Glaciation During the Cretaceous  
282 Supergreenhouse. *Science* **319**, 189–192 (2008).
- 283 11. Müller, R. D. et al. Long-Term Sea-Level Fluctuations Driven by Ocean Basin  
284 Dynamics. *Science* **319**, 1357–1362 (2008).
- 285 12. Miller, K. G. et al. The Phanerozoic Record of Global Sea-Level Change. *Science*  
286 **310**, 1293–1298 (2005).
- 287 13. Mcphail, M. K., Truswell, E. M. Palynology of Site 1166, Prydz Bay, East Antarctica.  
288 *In: Cooper, A. K., O'Brien, P. E. and Richter, C. (eds.) Proceedings of the Ocean*  
289 *Drilling Program, Scientific Results, College Station, TX (Ocean Drilling Program)*  
290 **188**, 1–43 (2004).
- 291 14. Mays, C., Steinthorsdottir, M. & Stilwell, J. D. Climatic implications of *Ginkgoites*  
292 *waarrensis* Douglas emend. from the south polar Tupuangi flora, Late Cretaceous  
293 (Cenomanian), Chatham Islands. *Palaeogeogr. Palaeoclimatol. Palaeoecol.* **438**,  
294 308–326 (2015).
- 295 15. Pujana, R. R., Raffi, M. E. & Olivero, E. B. Conifer fossil woods from the Santa Marta  
296 Formation (Upper Cretaceous), Brandy Bay, James Ross Island, Antarctica.  
297 *Cretaceous Research* **77**, 28–38 (2017).
- 298 16. Manfroi, J. et al. The first report of a Campanian palaeo-wildfire in the West Antarctic  
299 Peninsula. *Palaeogeogr. Palaeoclimatol. Palaeoecol.* **418**, 12–18 (2015).
- 300 17. Falcon-Lang, H. J., Cantrill, D. J. & Nichols, G. J. Biodiversity and terrestrial ecology  
301 of a mid-Cretaceous, high-latitude floodplain, Alexander Island, Antarctica. *J. Geol.*  
302 *Soc. Lond.* **158**, 709–724 (2001).
- 303 18. Wang, Y., Huang, C., Sun, B., Quan, C., Wu, J. & Lin, Z. Paleo-CO<sub>2</sub> variation trends  
304 and the Cretaceous greenhouse climate. *Earth-Sci. Rev.* **129**, 136–147 (2014).
- 305 19. Huber, B. T., MacLeod, K. G., Watkins, D. K. & Coffin, M. F. The rise and fall of the  
306 Cretaceous Hot Greenhouse climate. *Glob. Planet. Change* **167**, 1–23 (2018).
- 307 20. Arndt, J. E. et al. A new bathymetric compilation covering circum-Antarctic waters.  
308 *Geophys. Res. Lett.* **40**, 1–7 (2013).

- 309 21. Fretwell, P. et al. Bedmap2: improved ice bed, surface and thickness datasets for  
310 Antarctica. *The Cryosphere* **7**, 375–393 (2013).
- 311 22. Gohl, K. et al. MeBo70 seabed drilling on a polar continental shelf: operational report  
312 and lessons from drilling in the Amundsen Sea Embayment of West Antarctica.  
313 *Geochem. Geophys. Geosys.* **18**, 4235–4250 (2017).
- 314 23. Lowe, A. L. & Anderson, J. B. Reconstruction of the West Antarctic ice sheet in Pine  
315 Island Bay during the Last Glacial Maximum and its subsequent retreat history. *Quat.*  
316 *Sci. Rev.* **21**, 1879–1897 (2002).
- 317 24. Spiegel, C. et al. Tectonomorphic evolution of Marie Byrd Land – Implications for  
318 Cenozoic rifting activity and onset of West Antarctic glaciation. *Glob. Planet. Change*  
319 **145**, 98–115 (2016).
- 320 25. Larter, R. D. et al. Reconstruction of changes in the Amundsen Sea and  
321 Bellingshausen Sea sector of the West Antarctic Ice Sheet since the Last Glacial  
322 Maximum. *Quat. Sci. Rev.* **100**, 55–86 (2014).
- 323 26. Gohl, K. et al. Seismic stratigraphic record of the Amundsen Sea Embayment shelf  
324 from pre-glacial to recent times: Evidence for a dynamic West Antarctic ice sheet.  
325 *Mar. Geol.* **344**, 115–131 (2013).
- 326 27. Freudenthal, T. & Wefer, G. Drilling cores on the sea floor with the remote-controlled  
327 sea floor drilling rig MeBo. *Geoscientific Instrumentation, Methods and Data Systems*  
328 **2**, 329–337 (2013).
- 329 28. Crampton, J. S. et al. Cretaceous (Taitai, Clarence, Raukumara and Mata Series). In:  
330 Cooper, R.A. (Ed.), The New Zealand Geological Timescale. R. A. Cooper. Lower  
331 Hutt, Institute of Geological and Nuclear Sciences Limited. *Geological & Nuclear*  
332 *Sciences Monograph* **22**, 102–122 (2004).
- 333 29. Mays, C. & Stilwell, J. D. Pollen and spore biostratigraphy of the mid-Cretaceous  
334 Tupurangi Formation, Chatham Islands, New Zealand. *Rev. Palaeobot. Palynol.* **192**,  
335 79–102 (2013).

- 336 30. Mildenhall, D. C. Palynological reconnaissance of Early Cretaceous to Holocene  
337 sediments, Chatham Islands, New Zealand. *Institute of Geological & Nuclear*  
338 *Sciences monograph 7* in *New Zealand Geological Survey paleontological bulletin 67*,  
339 204 p. (1994).
- 340 31. He, T., Lamont, B. B. & Fogliani, B. Pre-Gondwanan-breakup origin of *Beauprea*  
341 (*Proteaceae*) explains its historical presence in New Caledonia and New Zealand,  
342 *Science Advances* **2**, E1501648 (2016).
- 343 32. Gee, J. & Kent, D. Source of Oceanic Magnetic Anomalies and the Geomagnetic  
344 Polarity Timescale. In: *Treatise on Geophysics*, vol. 5., Geomagnetism, Chapter 5.12,  
345 Elsevier, Editor: M. Kono, pp. 455-507, doi:10.1016/B978-044452748-6/00097-3  
346 (2007).
- 347 33. Wobbe, F., Gohl, K., Chambord, A. & Sutherland, R. Structure and breakup history of  
348 the rifted margin of West Antarctica in relation to Cretaceous separation from  
349 Zealandia and Bellingshausen plate motion. *Geochem. Geophys. Geosys.* **13**, 1–19  
350 (2012).
- 351 34. Jordan, T. A., Riley, T. R. & Siddoway, C. S. The geological history and evolution of  
352 West Antarctica. *Nature Reviews Earth & Environment*, doi:10.1038/s43017-019-  
353 0013-6 (2020).
- 354 35. Müller, R. D. et al. GPlates: Building a Virtual Earth Through Deep Time. *Geochem.*  
355 *Geophys. Geosys.* **19**, 2243–2261 (2018).
- 356 36. DiVenere, V. J., Kent, D. V. & Dalziel, I. W. D. Mid-Cretaceous paleomagnetic results  
357 from Marie Byrd Land, West Antarctica: A test of post-100 Ma relative motion  
358 between East and West Antarctica, *Journal of Geophysical Research* **99**, B8, 15115–  
359 15139 (1994).
- 360 37. Pocknall, D. T. & Crosbie, Y. M. Pollen morphology of *Beauprea* (*Proteaceae*):  
361 Modern and fossil. *Rev Palaeobot and Palynol* **53**, 305–327 (1988).

- 362 38. Jackson, M. B. & Armstrong, W. Formation of Aerenchyma and the Processes of  
363 Plant Ventilation in Relation to Soil Flooding and Submergence. *Plant Biol* **1**, 274–287  
364 (1999).
- 365 39. Lijmbach, G. W. M. On the origin of petroleum. *Proceedings of the 9th world*  
366 *petroleum congress* **2**, 357–369 (1975).
- 367 40. Peters, K. E., Walters, C. C. & Moldowan, J. M. The Biomarker Guide. *Cambridge*  
368 *University Press*, 1155 p. (2004).
- 369 41. Meyers, P. A. Applications of organic geochemistry to paleolimnological  
370 reconstructions: a summary of examples from the Laurentian Great Lakes. *Org.*  
371 *Geochem.* **34**, 261–289 (2003).
- 372 42. Robert, C. & Kennett, J. P. Antarctic subtropical humid episode at the Paleocene–  
373 Eocene boundary: Clay-mineral evidence. *Geology* **22**, 211–214 (1994).
- 374 43. Huang, W. H. & Keller, W. D. Dissolution of rock-forming silicate minerals in organic  
375 acids: Simulated first-stage weathering of fresh mineral surfaces. *The American*  
376 *Mineralogist* **55**, 2076–2094 (1970).
- 377 44. Sugden, D. E. & Jamieson, S. S. R. The pre-glacial landscape of Antarctica. *Scottish*  
378 *Geographical Journal* **134**, 203–223 (2018).
- 379 45. Uenzelmann-Neben, G. & Gohl, K. Early glaciation already during the Early Miocene  
380 in the Amundsen Sea, Southern Pacific: Indications from the distribution of  
381 sedimentary sequences. *Glob. Planet. Change* **120**, 92–104 (2014).
- 382 46. Zundel, M. et al. Thurston Island (West Antarctica) between Gondwana subduction  
383 and continental separation: A multistage evolution revealed by apatite  
384 thermochronology. *Tectonics* **38**, 878–897 (2019).
- 385 47. Müller, R. D., Gohl, K., Cande, S. C., Goncharov, A. & Golynsky, A. V. Eocene to  
386 Miocene geometry of the West Antarctic rift system. *Australian Journal of Earth*  
387 *Sciences* **54**, 1033–1045 (2007).



- 388 48. Harbert, R. S. & Nixon, K. C. Climate reconstruction analysis using coexistence  
389 likelihood estimation (CRACLE): A method for the estimation of climate using  
390 vegetation. *American Journal of Botany* **102(8)**, 1277–1289 (2015).
- 391 49. Poole, I., Cantrill, D. J. & Utescher, T. Reconstructing Antarctic palaeoclimate from  
392 wood floras: a comparison using multivariate anatomical analysis and the  
393 Coexistence Approach. *Palaeogeogr. Palaeoclimatol. Palaeoecol.* **222**, 95–121  
394 (2005).
- 395 50. Francis, J. E. et al. 100 million years of Antarctic climate evolution: evidence from  
396 fossil plants. In: Cooper, A. K. & Barrett, P. et al. (eds.) *Antarctica: A Keystone in a*  
397 *Changing World*. Proceedings of the 10<sup>th</sup> International Symposium on Antarctic Earth  
398 Sciences. USGS Santa Barbara, California, August 26 to September 1, 2007, The  
399 National Academies Press, Washington D.C., USA, pp. 19–27 (2007).
- 400 51. Bauersachs, T., Rochelmeier, J. & Schwark, L. Seasonal lake surface water  
401 temperature trends reflected by heterocyst glycolipid-based molecular thermometers.  
402 *Biogeosciences* **12**, 3741–3751 (2015).
- 403 52. Ladant, J. L. & Donnadieu, Y. Paleogeographic regulation of glacial events during the  
404 Cretaceous supergreenhouse. *Nat. Comm.* **7**, doi:10.1038/ncomms12771, (2016).
- 405 53. Upchurch, G. R. jr., Kiehl, J., Shields, C., Scherer, J. & Scotese, C. Latitudinal  
406 temperature gradients and high-latitude temperatures during the latest Cretaceous:  
407 Congruence of geologic data and climate models. *Geology* **43**, 683–686 (2015).
- 408 54. Farnsworth, A. et al. Climate sensitivity on geological timescales controlled by non-  
409 linear feedbacks and ocean circulation. *Geophys. Res. Lett.* **46**,  
410 doi:10.1029/2019GL083574 (2019).
- 411 55. IPCC. IPCC Special Report on the Ocean and Cryosphere in a Changing Climate.  
412 Pörtner, H. O. et al. (eds.), in press.  
413 [https://www.ipcc.ch/site/assets/uploads/sites/3/2019/12/SROCC\\_FullReport\\_FINAL.p](https://www.ipcc.ch/site/assets/uploads/sites/3/2019/12/SROCC_FullReport_FINAL.pdf)  
414 [df](https://www.ipcc.ch/site/assets/uploads/sites/3/2019/12/SROCC_FullReport_FINAL.pdf) (2019).
- 415

416 Supplementary Video 1: 3D animation video of the sediment record. Animated video from X-  
417 ray computed tomography (CT) data of cores PS104\_20-2 9R and 10R.

418

#### 419 *Acknowledgements*

420 We thank captain and crew of RV *Polarstern* Expedition PS104, as well as the MARUM-  
421 *MeBo70* team for their support. The operation of the *MARUM-MeBo70* Sea Floor Drill Rig  
422 was funded by the Alfred Wegener Institute (AWI) through its Research Program PACES II  
423 Topic 3 and grant no. AWI\_PS104\_001, the MARUM Center for Marine Environmental  
424 Sciences, the British Antarctic Survey through its Polar Science for Planet Earth programme,  
425 and the Natural Environmental Research Council funded UK IODP programme. S. Wiebe, R.  
426 Fröhling, V. Schumacher, N. Lensch, M. Arevalo, M. Seebeck, and H. Grobe are thanked  
427 for their help on board and in the lab, respectively. The *Klinikum Bremen-Mitte* (A.-J. Lemke  
428 and C. Tiemann, *Gesundheit Nord* Bremen) is acknowledged for providing facilities for  
429 computed core tomographies, and M. Köhler (MKfactory, Germany) for preparing the thin  
430 sections. J. McKay (University of Leeds) is thanked for creating and painting the Late  
431 Cretaceous West Antarctic palaeoenvironment based on reconstructions presented here.  
432 J.P.K, G.K., K.G., J.M. G.U.-N., O.E., C.G., T.R. and R.D. were funded by the AWI PACES II  
433 programme. J.P.K. and J.M. were additionally funded through the Helmholtz Association  
434 (PD-201 & VH-NG-1101). UK IODP funded participation of T.v.d.F., P.S.P. and S.M.B. in  
435 expedition PS104. J.T. was funded through the Cluster of Excellence “The Ocean Floor –  
436 Earth’s Uncharted Interface” at the University of Bremen.

437

#### 438 *Author contributions*

439 J.P.K. led the study and together with U.S., T.B., C.-D.H., K.G. and G.K., conceived the idea  
440 for the study and wrote the manuscript. J.P.K, T.B., C.-D.H., S.B., J.A.S., K.G., T.F, T.v.d.F.,  
441 P.S.P., W.E., O.E., H.P. and T.R. collected the cores. J.P.K, C.-D.H., T.B. and G.K.  
442 undertook the sedimentological and U.S. and S.B. the palynological analyses. T.B. and G.K.  
443 conducted the XRF scanning and processing of the cores. G.K. carried out the grain-size and

444 bulk mineralogical analyses. J.T. led the CT scanning, processing, and visualization. J.M.  
445 performed the biomarker analyses together with Th.B. (heterocyst glycolipid  
446 palaeothermometry). T.F. conducted the palaeomagnetic measurements. J.E.F., G.N., G.K.  
447 and J.P.K. investigated the thin sections. W.E. analysed the clay mineral assemblages and  
448 T.v.d.F. and P.S.P. measured bulk sediment Nd and Sr isotope compositions. K.G., R.D.L.,  
449 and T.F. helped determining the palaeolatitude of the drill site. G.L. and I.N. undertook the  
450 modelling with COSMOS. M.Z., C.S., C.M. and D.C. provided the U/Pb age constraints. U.S.  
451 and F.S. performed the bioclimatic analyses. J.P.K., T.B., C.-D.H., S.B., T.F., W.E., J.A.S.,  
452 O.E., O.E., H.P., T.R. and R.D. helped sampling and scanning the cores. K.G., G.U.-N. and  
453 R.D.L. undertook the seismic pre-site survey. All members of the Expedition PS104 Science  
454 Team helped in pre-site survey investigations, core recovery, on-board analyses and/or  
455 shore-based measurements. K.G., G.K., C.-D.H., G.U.-N., T.B. and R.D.L. acquired funding,  
456 proposed, and planned RV *Polarstern* expedition PS104. All co-authors commented on the  
457 manuscript and provided input to its final version.

458

#### 459 *Author information*

460 Reprints and permissions information is available at [www.nature.com/reprints](http://www.nature.com/reprints). The authors  
461 declare no competing financial interests. Readers are welcome to comment on the online  
462 version of the paper. Correspondence and requests for materials should be addressed to  
463 J.P.K. (Johann.Klages@awi.de).

464

#### 465 **Science Team of Expedition PS104**

466 Afanasyeva, V., VNIIOkeangeologie, St. Petersburg, Russia

467 Arndt, J. E., Alfred-Wegener-Institut, Helmholtz-Zentrum für Polar- und Meeresforschung,  
468 Bremerhaven, Germany

469 Ebermann, B., Technische Universität Dresden, Dresden, Germany

470 Gebhardt, C., Alfred-Wegener-Institut, Helmholtz-Zentrum für Polar- und Meeresforschung,  
471 Bremerhaven, Germany

472 Hochmuth, K., Alfred-Wegener-Institut, Helmholtz-Zentrum für Polar- und Meeresforschung,  
473 Bremerhaven, Germany, now at: School of Geology, Geography and the Environment,  
474 University of Leicester, Leicester, UK

475 Küssner, K., Alfred-Wegener-Institut, Helmholtz-Zentrum für Polar- und Meeresforschung,  
476 Bremerhaven, Germany

477 Najman, Y., Lancaster Environment Centre, Lancaster University, Lancaster, UK

478 Riefstahl, F., Alfred-Wegener-Institut, Helmholtz-Zentrum für Polar- und Meeresforschung,  
479 Bremerhaven, Germany

480 Scheinert, M., Technische Universität Dresden, Dresden, Germany

481

482 *Figure captions*

483 Figure 1: Setting of *MARUM-MeBo70* drill site PS104\_20-2 on the Amundsen Sea

484 Embayment (ASE) shelf. a) The modern configuration of West Antarctica is placed in relation  
485 to the reconstructed boundary between continental and oceanic crust (COB) at 84 Myr<sup>33,34</sup>  
486 (thick black lines). The pre-break up suture (dashed white line) indicates the position of the  
487 reconstructed Zealandian and West Antarctic COBs prior to initial break-up starting at ~90  
488 Myr<sup>33</sup>. Orange circles mark the locations of other outcrops of mid-Cretaceous sedimentary  
489 strata<sup>13-17</sup>. b) Seismic reflection profile NBP9902-11<sup>23</sup> (A-B) crossing drill site 20-2: orange  
490 bar indicates drilled core length. The profile position is indicated in "a". The drill hole  
491 penetrated Amundsen Sea shelf unconformity ASS-u1, which separates seismic units ASS-1  
492 and ASS-2<sup>26</sup>. Interpretation of seismostratigraphic units and unconformities is based on both  
493 previous work<sup>26</sup> and this study. Pitt Island belongs to the Chatham Island group of New  
494 Zealand. PB: Prydz Bay; ChR: Chatham Rise. Shelf bathymetry and sub-ice topography data  
495 derive from refs. 20 and 21.

496

497 Figure 2: Multi-proxy parameter reconstruction of cores 9R and 10R at site PS104\_20-2. The  
498 *MARUM-MeBo70* sea floor drill rig drilled 30.7 m into the seafloor and recovered 5.91 m of  
499 core length. The lower ~3 m consist of a fossil root-bearing mudstone with a ~5 cm-thin layer

500 of brecciated lignite on top (from ~26.77 mbsf downwards) both of Turonian–Santonian age.  
501 A Late Eocene or younger quartzitic sandstone overlies the lignite. The upper lignite  
502 boundary defines the impedance contrast between the underlying mudstone and overlying  
503 quartzitic sandstone and likely coincides with the prominent regional unconformity ASS-u1<sup>26</sup>  
504 (see thick red line in Fig. 1b). Note the core break between 9R and 10R at 27.15 mbsf. (LS:  
505 Linescan; CT: X-Ray computed tomography; Cl/St/Sd: Clay/Silt/Sand; TOC: Total organic  
506 carbon; Gy/An/Pt/Br: Gymnosperms/Angiosperms/Pteridophytes/Bryophytes; x: Barren  
507 palynomorph samples; Fe(Ca): Iron-carbonate; Bulk sediment neodymium ( $\epsilon_{Nd}$ ) values ( $\pm 2$   
508 S.D. = 0.27) and strontium ( $^{87}Sr/^{86}Sr$ ) ratios ( $\pm 2$  S.E. = see Source data) (see Methods); TAR:  
509 Ratio of terrestrial and aquatic-sourced *n*-alkanes; C:N (mol.): molar ratio of total organic  
510 carbon (TOC) to total nitrogen (TN); \*: Zircon U-Pb age (45.5 Myr); mbsf: meters below sea  
511 floor). Inferred ages are based on palynomorph biostratigraphy for the mudstone and U/Pb  
512 ages of apatite and zircon grains for the sandstone (see text). Data link to PANGAEA (DOI in  
513 progress): <https://doi.pangaea.de/10.1594/PANGAEA.906092>.

514

515 Figure 3: Modern and mid-Cretaceous CO<sub>2</sub> sensitivity runs. Distribution of warmest mean  
516 month temperatures (WMMT) (°C) for present (upper row: a-c) and mid-Cretaceous at 90  
517 Myr (lower row: d-f) configurations for atmospheric CO<sub>2</sub> levels of 280, 560, 1120 ppm,  
518 representing 1x, 2x and 4x pre-industrial CO<sub>2</sub> level of 280 ppm. The black triangle indicates  
519 the approximate position of site PS104\_20-2 (a–c: modern; d–f: Turonian–Santonian). g)  
520 Modelled mid-Cretaceous WMMT (dashed coloured lines) and zonal mean temperatures (full  
521 coloured lines) for different atmospheric CO<sub>2</sub> concentrations. The temperature estimates,  
522 including their respective calibration error ( $2\sigma$ ), were derived from the following proxies  
523 referred to in ref. 5: terrestrial  $\delta^{18}O$  of vertebrate tooth enamel and/or pedogenic carbonate  
524 (full squares), palaeobotanical data (full circles), fish enamel  $\delta^{18}O$  (open triangles), marine  
525 calcareous fossil  $\delta^{18}O$  (open diamonds), and biomarkers (cross). Temperature estimates  
526 from this study are indicated as a red full circle and cross, respectively.

527

528 Figure 4: Visual reconstruction of the West Antarctic Turonian–Santonian temperate  
529 rainforest. The painting is based on palaeo-floral and environmental information inferred from  
530 palynological, geochemical, sedimentological, and organic biomarker data obtained from  
531 cores 9R and 10R at site PS104\_20-2. The creation of the painting was further  
532 complemented by published palaeo–topographic and palaeo–tectonic information<sup>24,26,33,34</sup>.  
533 Original size of painting: 83.8 x 41.5 cm. Alfred-Wegener-Institut/J. McKay; this image is  
534 available under Creative Commons licence CC-BY 4.0.

535

536 *Methods*

### 537 **Sea Floor Drill Rig *MARUM-MeBo70***

538 The sea floor drill rig *MARUM-MeBo70* is a robotic drill rig that was deployed on the seabed  
539 and remotely controlled from RV *Polarstern* during expedition PS104<sup>22</sup>. Detailed information  
540 about the drill rig and its operation is published in ref. 27.

541

### 542 **X-ray computed tomography**

543 Whole rounds of *MeBo* core PS104\_20-2 were scanned by a *Toshiba Aquilion 64*<sup>TM</sup>  
544 computer tomograph (CT) at the hospital *Klinikum Bremen-Mitte*, with an X-ray source  
545 voltage of 120 kV and a current of 600 mA. The CT scans have a resolution of 0.351 mm in  
546 x- and y-direction and 0.5 mm resolution in z-direction (resolution of scaled reconstruction:  
547 0.195 x 0.195 x 0.3 mm). Images were reconstructed using Toshiba's patented helical cone  
548 beam reconstruction technique. The obtained CT data were processed using the ZIB edition  
549 of the *Amira* software (version 2017.39)<sup>56</sup>. Within *Amira*, the CT scans of the core sections  
550 were merged when necessary and core liners, including about 2 mm of the core rims, were  
551 removed from the dataset until all marginal artefacts from the coring process were removed.  
552 Subsequently, all clasts > ~1 mm, root-traces (where present) and matrix sediment were  
553 segmented with the (marker-based) watershed tool of the *Segmentation Editor*. Markers  
554 were predominantly set by density thresholding. Holes within clasts after the watershed

555 segmentation were added to the clasts with the *selection fill* tool. Only in exceptional cases,  
556 markers were segmented by hand.

557

### 558 **Palynology**

559 Between 2 and 6 g of dry weight sediment per sample were processed at Northumbria  
560 University, following standard palynological techniques, including sieving (10 µm) and acid  
561 treatment with 10% HCl (Hydrochloric acid) and cold 38% HF (Hydrofluoric acid). The  
562 processed residue was transferred to microscope slides using glycerine jelly as a mounting  
563 medium, and 2–3 slides were analysed per sample at 400x magnification. Of the 17 samples  
564 analysed for pollen and spores, 7 were productive, and total counts range from 340 to 360  
565 pollen and spores per sample (Extended Data Figs. 2, 3; Extended Data Table 1). Pollen  
566 concentrations increase from an average of ~6,500 grains/g sediment in the lower three  
567 samples to 61,000–121,500 grains/g at the top. We could not identify any reworking of  
568 palynomorphs. Percentages were calculated based on the sum of total pollen and spores. 65  
569 pollen and spore taxa were identified from the literature<sup>57–59</sup> (Extended Data Table 3). All  
570 samples contained a high morphological diversity of *Podocarpus* pollen, which we classified  
571 as *Podocarpidites* undiff., as many of these grains were either folded or damaged and were  
572 therefore unidentifiable beyond family level. Marine dinoflagellate cysts were absent in all  
573 samples.

574

### 575 **Palynomorph-based climate reconstructions (Bioclimatic analysis)**

576 We reconstructed terrestrial mean annual temperature (MAT), precipitation (MAP) and mean  
577 warmest month temperature (WMMT) using the Nearest Living Relative (NLR) approach.  
578 The NLR approach uses the climatic requirements of the NLR of fossil taxa to reconstruct the  
579 past climatic range and assumes that the climatic requirements of the fossil taxa are similar  
580 to those of their NLR (Extended Data Table 2). NLR approaches use the presence or  
581 absence of individual taxa in fossil assemblage rather than relative abundance, which  
582 reduces the likelihood of taphonomic biases. This facilitates, to some extent, the

583 reconstruction of past non-modern analogue climates and environments<sup>60</sup>. NLR-based  
584 temperature estimates are generally in good agreement with estimates from geochemical  
585 and other palaeobotanical methods, including the Climate Leaf Analysis Multivariate Program  
586 (CLAMP) and Leaf Margin Analysis<sup>61–67</sup> providing confidence in the utility of the method for  
587 the reconstruction of “deep-time” climates.

588 However, quantitative climate estimates from the fossil plant record of “deep-time” geological  
589 intervals are always accompanied by large uncertainties. Incorrect use of outliers and fossil  
590 taxa with ambiguous affinity can result in erroneous climate estimates<sup>68</sup>. One of the greatest  
591 weaknesses that affects all NLR approaches is the assumption of uniformitarianism, namely  
592 that the climate tolerances of modern species can be extended into the past. This  
593 assumption inevitably introduces uncertainty that increases with the age of the geological  
594 formation<sup>69</sup>. In order to statistically constrain the most likely climatic co-occurrence envelope,  
595 we combined the NLR approach with the probability density function (PDF) method<sup>70–72</sup>. In  
596 contrast to other NLR methods, such as the Coexistence Approach, the PDF method has the  
597 advantage that it statistically constrains the most likely climatic co-occurrence envelope,  
598 thereby offering a solution to mathematically reduce the potential impact of wrongly defined  
599 climate tolerance on upper and lower limits of palaeoclimatic estimates. In order to further  
600 reduce uncertainties caused by potentially wrong identification of NLR, we removed fossil  
601 taxa with potentially ambiguous affinity or very rare occurrence in the fossil record (Extended  
602 Data Table 2). This includes *Microcachrydites antarcticus*, a taxon abundant and widespread  
603 in the fossil Antarctic record, with the NLR *Microcachrys tetragona*, the sole species of the  
604 genus *Microcachrys*, that nowadays is endemic to Tasmania. Another example is  
605 *Peninsulapollis gillii* with close links to the modern genus *Beauprea*, and endemic to New  
606 Caledonia. In both cases we used the family, Podocarpaceae and Proteaceae, respectively,  
607 rather than the genus or species as the NLR.

608 To generate the paleoclimate estimate, we followed the procedure described in refs. 59 and  
609 63. We first identified the bioclimatic envelope for each NLR by cross-plotting their modern  
610 distribution from the Global Biodiversity Information Facility (GBIF)<sup>73</sup> with the gridded



611 WorldCLIM climate surface<sup>74</sup> using the “dismo” package<sup>75</sup> in R. We then filtered the dataset  
 612 and removed redundant data, “exotic” occurrences (such as garden plants) as well as  
 613 multiple entries per climate grid cell to avoid the climatic probability function becoming highly  
 614 slanted towards that location<sup>76</sup>. Before establishing the probability density functions,  
 615 bootstrapping was applied to test the robustness of the dataset, which is of particular interest  
 616 for taxa with only few modern occurrences. Following the bootstrapping, we calculated the  
 617 likelihood (f) of a taxon (t) occurring at value (x) for a certain climatic variable by using the  
 618 mean ( $\mu$ ) and standard deviation ( $\sigma$ ) of the modern distribution range of each taxa<sup>65,70</sup>.

$$f(x)_t = \frac{1}{\sqrt{2\pi\sigma_x^2}} e^{-\frac{(x-\mu_x)^2}{2\sigma_x^2}}$$

619

620 Since the separate reconstruction of climate ranges for each variable can lead to bioclimatic  
 621 envelopes that include intervals, where no modern-day occurrence of taxon t is observed<sup>65</sup>,  
 622 we calculated joint likelihood PDFs for each combination of climate variables MAT, MAP and  
 623 WMMT using the correlation coefficient p (x, y):

624

$$f(x, y)_t = \frac{1}{2\pi\sigma_x\sigma_y\sqrt{1-p^2}} e^{-\frac{1}{2(1-p^2)}\left(\frac{(x-\mu_x)^2}{2\sigma_x^2} + \frac{(y-\mu_y)^2}{2\sigma_y^2} - 2p\frac{(x-\mu_x)(y-\mu_y)}{\sigma_x\sigma_y}\right)}$$

625

626 After assessing if all bioclimatic envelopes share a coexistence interval, the climate  
 627 estimates of the NLR assemblage were reconstructed by multiplying the individual joint  
 628 likelihoods of taxa  $f(x, y)_{t1} \dots f(x, y)_{tn}$  with each other:

629

$$f(x, y)_{combined} = f(x, y)_{t1} \times f(x, y)_{t2} \times \dots \times f(x, y)_{tn}$$

630

631 In order to constrain the core distribution of a group, we determined the range of one ( $f(x,$   
 632  $y)_{relative} = 0.157$ ) and two standard deviations ( $f(x, y)_{relative} = 0.023$ ) from the occurrence within  
 633 a group with  $f(x, y)_{max}$  representing the most likely climate conditions<sup>76</sup>.

634

$$f(x,y)_{relative} = \frac{f(x,y)}{f(x,y)_{max}}$$

635

636 For our bioclimatic analysis we used all pollen and spore taxa that could be related to an  
 637 NLR, following ref. 59 (Extended Data Table 2). Climatic ranges are indicated with their  $\pm 2 \sigma$   
 638 range. For our record we calculated mean annual temperatures of  $12.8 \pm 2.2^\circ\text{C}$ , warmest  
 639 mean month temperatures of  $18.4 \pm 1.9^\circ\text{C}$ , and mean annual precipitation of  $1,120 \pm 330$   
 640 mm/a. It should be noted that the ranges of these values show the mathematical error and  
 641 not the real range, which might result from the uncertainties of using an NLR approach  
 642 method. To avoid misunderstandings, we therefore indicated in the main text the pollen-  
 643 based climate estimates without  $2 \sigma$  ranges.

644

#### 645 **Organic geochemistry**

646 Freeze-dried and homogenized sediment samples were extracted by means of  
 647 ultrasonication using a dichloromethane:methanol mixture (2:1, v:v). After centrifugation, the  
 648 total lipid extract was dried by rotary evaporation. The extraction was repeated twice. The  
 649 combined total lipid extract was fractionated using silica open-column chromatography and  
 650 hexane as eluent to obtain apolar lipids. Hydrocarbons were analysed using an HP gas  
 651 chromatograph 6890 (30 m DB-5MS column, 0.25 mm diameter, 0.25  $\mu\text{m}$  film thickness).  
 652 The identification of *n*-alkanes, pristane, and phytane was based on comparison of their  
 653 retention times with those of reference compounds that were run on the same instrument.  
 654 The terrigenous-aquatic-ratio (TAR<sup>77</sup>) was calculated using peak areas of long-chain (*n*-C<sub>27</sub>,  
 655 *n*-C<sub>29</sub>, *n*-C<sub>31</sub>) against short-chain (*n*-C<sub>15</sub>, *n*-C<sub>17</sub>, *n*-C<sub>19</sub>) alkanes. The carbon preference index  
 656 (CPI) was calculated as follows<sup>40</sup>:

657

$$658 \quad (1) \text{ CPI} = 2 * (n\text{-C}_{23} + n\text{-C}_{25} + n\text{-C}_{27} + n\text{-C}_{29}) / (n\text{-C}_{22} + 2 * (n\text{-C}_{24} + n\text{-C}_{26} + n\text{-C}_{28}) + n\text{-C}_{30}).$$

659

#### 660 **Heterocyst glycolipid palaeothermometry**

661 Sediment samples from the coastal sandstone (9R, 50-52 cm; 2676 cmbsf) and the  
662 carbonaceous mudstone (9R, 76.5–78 cm; 27.02 mbsf; 10R, 60–62 cm; 29.21 mbsf) were  
663 lyophilized and ground to fine sediment powder using a solvent-cleaned agate pestle and  
664 mortar. Between 20.1 and 29.7 g of sediment was extracted using a modified Bligh and Dyer  
665 procedure<sup>78</sup>. Briefly, the cell material was extracted ultrasonically thrice for 10 min each in a  
666 solvent mixture of MeOH, DCM and phosphate buffer (2:1:0.8; v:v:v). After each sonication  
667 step, the solvent mixture was centrifuged at 1,500 x g for 3 min and the supernatant  
668 transferred to a centrifuge tube. The combined supernatants were phase separated by  
669 adding DCM and phosphate buffer to a final solvent ratio of 1:1:0.9 (v:v:v). The organic  
670 bottom layer was collected in a round bottom flask and reduced under vacuum using a rotary  
671 evaporator. Each Bligh and Dyer extract (BDE) was transferred to a pre-weighed vial using  
672 DCM:MeOH (1:1, v:v) and dried under a gentle stream of N<sub>2</sub>. Prior to analysis, all BDEs were  
673 re-dissolved in a solvent mixture of *n*-hexane:2-propanol:H<sub>2</sub>O (72:27:1; v:v:v) to a  
674 concentration of 8 mg/ml. In order to test for possible cross contamination during sample  
675 preparation a blank was included in each batch and treated as a regular sample.  
676 High performance liquid chromatograph coupled to electrospray ionisation tandem mass  
677 spectrometry (HPLC/ESI-MS<sup>2</sup>) was performed on the BDEs following the analytical  
678 procedure given by ref. 79 to establish heterocyst glycolipid (HG) distribution patterns and  
679 relative abundances. Separation of HGs was achieved using a Waters Alliance 2690 HPLC  
680 system fitted with a Phenomenex Luna NH<sub>2</sub> column (150 × 2 mm; 3 μm particle size) and a  
681 guard column of the same material. Both were maintained at a constant temperature of 30°C.  
682 The applied gradient profile was as follows: 95% A/5% B to 85% A/15% B in 10 min.  
683 (isocratic for 7 min) at 0.5 ml min<sup>-1</sup>, followed by back flushing with 30 % A/70% B at 0.2 ml  
684 min<sup>-1</sup> for 25 min. and re-equilibrating the column with 95% A/5% B for 15 min. Solvent A was  
685 *n*-hexane:2-propanol:HCO<sub>2</sub>H:14.8 M NH<sub>3</sub> aq. (79:20:0.12:0.04; v:v:v:v) and Solvent B was 2-  
686 propanol:water:HCO<sub>2</sub>H:14.8 M NH<sub>3</sub> aq. (88:10:0.12:0.04; v:v:v:v).  
687 Heterocyst glycolipids were detected using a Micromass Quattro LC triple quadruple mass  
688 spectrometer equipped with an electrospray ionisation (ESI) interface and operated in

689 positive ion mode. Source conditions were as given in ref. 80. All BDEs were analysed in  
690 multiple reaction monitoring (MRM) mode to achieve maximum specificity and HGs identified  
691 based on comparison of retention times with those of HGs in cultured cyanobacteria as well  
692 as published mass spectral information<sup>81–85</sup>. HGs were monitored using the following  
693 transitions:  $m/z$  547  $\rightarrow$  415 (pentose HG<sub>26</sub> diol),  $m/z$  603  $\rightarrow$  471 (pentose HG<sub>30</sub> diol),  $m/z$  619  
694  $\rightarrow$  487 (pentose HG<sub>30</sub> triol),  $m/z$  647  $\rightarrow$  515 (pentose HG<sub>32</sub> triol),  $m/z$  561  $\rightarrow$  415  
695 (deoxyhexose HG<sub>26</sub> diol),  $m/z$  575  $\rightarrow$  413 (HG<sub>26</sub> keto-ol),  $m/z$  577  $\rightarrow$  415 (HG<sub>26</sub> diol),  $m/z$  603  
696  $\rightarrow$  441 (HG<sub>28</sub> keto-ol),  $m/z$  605  $\rightarrow$  443 (HG<sub>28</sub> diol),  $m/z$  619  $\rightarrow$  457 (HG<sub>28</sub> keto-diol),  $m/z$  621  
697  $\rightarrow$  459 (HG<sub>28</sub> triol),  $m/z$  635  $\rightarrow$  459 (methylated hexose HG<sub>28</sub> triol),  $m/z$  647  $\rightarrow$  485 (HG<sub>30</sub>  
698 keto-diol),  $m/z$  649  $\rightarrow$  487 (HG<sub>30</sub> triol),  $m/z$  675  $\rightarrow$  513 (HG<sub>32</sub> keto-diol),  $m/z$  677  $\rightarrow$  515 (HG<sub>32</sub>  
699 triol) and quantified by integrating peak areas using the QuanLynx application software.  
700 Surface water temperatures (SWTs) during the deposition of the coastal Eocene sandstone  
701 were re-constructed using the HDI<sub>26</sub> (heterocyst diol index of 26 carbon atoms) and HDI<sub>28</sub>  
702 (heterocyst diol index of 28 carbon atoms) lipid palaeothermometers as described by ref. 51.  
703 As the HG content of the swampy palaeoenvironment exclusively consisted of HG<sub>30</sub> triols  
704 and HG<sub>30</sub> keto-diol (Extended Data Fig. 4), which are specific for cyanobacteria forming  
705 benthic microbial mats<sup>83</sup>, we here applied the HTI<sub>30</sub> (heterocyst triol index of 30 carbon  
706 atoms) to the mudstone sequence. This index is defined as follows:

$$707 \quad \text{HTI}_{30} = \text{HG}_{30} \text{ triol} / (\text{HG}_{30} \text{ triol} + \text{HG}_{30} \text{ keto-diol})$$

708 The HTI<sub>30</sub> was transferred to absolute temperatures using a surface sediment calibration  
709 obtained from a large set of East African lakes ( $n = 47$ ) located on an altitudinal transect from  
710 615 to 4504 masl and SWTs ranging from 5.7 to 27.9°C. In this setting, the HTI<sub>30</sub> showed a  
711 strong linear correlation with SWT, which is expressed in the equation below (Bauersachs,  
712 unpublished data):

$$713 \quad \text{SWT} = (\text{HTI}_{30} / 0.0249) - (0.2609 / 0.0249)$$

714 Independent conformation for the robustness of the HG-based temperature reconstruction is  
715 obtained by comparing HG distribution patterns and HTI<sub>30</sub> values in the mudstone sequence  
716 with those reported for an axenic culture of the heterocystous cyanobacterium *Scytonema*  
717 sp. PCC 10023 (ref. 85). This cyanobacterium exclusively contains HG<sub>30</sub> triols and HG<sub>30</sub>  
718 keto-diols. The above transfer function predicts a HTI<sub>30</sub> of ~0.88 for the culture grown at an  
719 ambient temperature of 25°C, which is in the same order of magnitude as the HTI<sub>30</sub>  
720 calculated using the relative abundances of the major HG<sub>30</sub> triol and HG<sub>30</sub> keto-diol isomers  
721 reported in ref. 85.

722

### 723 **Grain-size analyses**

724 A set of discrete samples was wet sieved at 2 mm and 63 µm to separate the grain-size  
725 classes gravel, sand, and mud. The < 63 µm (mud) suspension was separated into silt (2 to  
726 63 µm) and clay (< 2 µm) using settling velocity (Stokes' Law) in Atterberg tubes.

727

### 728 **Clay mineral analyses**

729 An aliquot of the clay fraction was used to determine the relative contents of the clay  
730 minerals smectite, illite, chlorite, and kaolinite using an automated powder diffractometer  
731 system Rigaku MiniFlex with CoKα radiation (30 kV, 15 mA) at the Institute for Geophysics  
732 and Geology (University of Leipzig). The clay mineral identification and quantification  
733 followed standard X-ray diffraction methods<sup>86</sup>.

734

### 735 **Bulk sediment composition**

736 Total carbon (TC) and total nitrogen (TN) were analysed with an Elementar Vario EL III. Total  
737 organic carbon (TOC) contents were determined after removal of the total inorganic carbon  
738 (TIC, carbonates) with HCl using an ELTRA CS-2000. Carbonate content was calculated by  
739 subtracting the TOC from the TC and multiplying the difference (TIC) by 8.33, i.e. the ratio  
740 between the molecular weights of CaCO<sub>3</sub> and C. The TOC:TN (C:N) ratio was calculated on  
741 a molar basis.

742 The mineralogical composition of the milled bulk sediment was analysed semi-quantitatively  
743 with X-ray diffraction using peak intensities and area ratios analysed with the MacDiff  
744 program<sup>87</sup>. For the Fe(Ca)-carbonates the peak intensities for ankerite (at 2.9 Å) and siderite  
745 (at 2.791 Å) were used and summed up as percentages for Fe(Ca)-carbonates (ankerite and  
746 siderite) in relation to the absolute % of other carbonates (calcite, Mg-calcite, and dolomite).

747

#### 748 **Thin sections**

749 After drying the untreated soft sediment in the fridge for 2–3 days, the sediment was dried at  
750 room temperature (20–22°C) for another 2–3 days. During that time the sediment was  
751 checked daily for crack formation. Under low pressure, the sediment was impregnated  
752 stepwise in a vacuum exicator with epoxy araldite 2020 resin until full coverage of the  
753 sample. After complete hardening, the bottom of the sample was ground by a Tegrapol with  
754 silicon carbid (SiC) paper sizes from 80 to 800 – depending on sediment characteristics –  
755 and a maximum of 150 rotations per minute until reaching the sediment surface. The glasses  
756 for covering the thin sections with a thickness of 3 mm and a diameter of 35x120 mm were  
757 ground with a 9-micron fraction SiC paper to achieve both grip and an even surface  
758 (alternative machine system: Logitech LP50 auto). Then the sample was attached to the  
759 glass with the same resin used for impregnation by a pressure block. Afterwards, the surface  
760 of the glass was cleaned and labelled with a diamond pen. Most samples were then cut by a  
761 WOCO 50 diamond saw for achieving 250 µm-thick sediment stripes on the glass, before  
762 grounding with SiC paper or the Logitech LP50 to reach a thickness of 30 µm. Some  
763 sections were covered with 150 µm-thick glasses, for which an ultraviolet resin (cyanacrylate)  
764 was used. Most sections remained uncovered for Raman and SEM-EDX spectroscopy.  
765 Finally, all thin sections were cleaned with ethanol. The set of thin sections was prepared by  
766 MKfactory (Stahnsdorf, Germany).

767

#### 768 **Palaeomagnetic measurements**

769 Five discrete samples were taken with variable spacing from cores 9R and 10R of core  
770 PS104\_20-2 for palaeomagnetic investigations using plastic boxes with inner dimensions of  
771 2×2×2 cm. Directions and intensities of natural remanent magnetization (NRM) were  
772 measured on a cryogenic magnetometer (model 2G Enterprises 755 HR). Subsequent  
773 alternating field demagnetization of NRM involved 15 steps to a maximum AF intensity of 100  
774 mT. A detailed vector analysis<sup>88</sup> was applied to the results in order to determine the  
775 characteristic remanent magnetization (ChRM) of each sample and to unravel its magnetic  
776 polarity. Samples showing no systematic demagnetization pattern were excluded from further  
777 interpretation.

778

### 779 **Palaeoclimate modelling**

780 We use the COSMOS model (see Code availability) in a coupled atmosphere-ocean  
781 configuration with fixed vegetation. The atmosphere component ECHAM5 is run in a T31/L19  
782 resolution<sup>89</sup>. It consists of 19 vertical layers and has a horizontal resolution of ~3.75°. The  
783 ocean component MPI-OM runs in GR30/L40 configuration<sup>90</sup>. It has a formal horizontal  
784 resolution of 3.0° x 1.8° and consists of 40 unequal vertical layers. The high-resolution  
785 hydrological discharge model is a part of ECHAM5<sup>91</sup> while MPI-OM includes a dynamic-  
786 thermodynamic sea-ice model utilizing a viscous-plastic rheology<sup>92</sup>. Climate simulations were  
787 run for present and mid-Cretaceous configurations under different CO<sub>2</sub> levels in the  
788 atmosphere. Other greenhouse gases (such as CH<sub>4</sub> and N<sub>2</sub>O) were set to pre-industrial (PI)  
789 level. In the mid-Cretaceous simulations, we employ published paleogeography<sup>93</sup> and  
790 vegetation<sup>94</sup> as well as no ice sheets on both hemispheres. The orbital configurations in all  
791 Cretaceous experiments were fixed at 800 common era (CE) and hence represent values  
792 from the beginning of externally forced simulation from 800 to 1,800 CE (so called millennial  
793 run). The solar constant was reduced by 1% for the mid-Cretaceous experiments relative to  
794 the present-day value. The simulations with 1x and 2x PI CO<sub>2</sub> levels were run for 9,200 and  
795 9,000 years, respectively, while 10,600 years for 4x PI CO<sub>2</sub> (ref. 95). All simulations reached  
796 equilibrium at the surface. The experiment with 6x PI CO<sub>2</sub> level had a slightly different

797 atmospheric land-sea mask than the other three simulations. It was run for ~500 years and  
798 was not in a full equilibrium at the surface<sup>5</sup>. The pre-industrial control simulation was run for  
799 ~7,500 years. The simulations with 2x and 4x PI CO<sub>2</sub> levels were branched off from 1x PI  
800 simulation from the year 6,800 and were further run for 700 years. The simulations reach  
801 either full or quasi equilibrium at the surface. For the analyses the mean was taken over the  
802 last 100 years of each simulation. The model has been successfully applied previously for  
803 scientific questions focusing on the Quaternary<sup>96,97</sup>, Neogene<sup>98–100</sup>; Palaeogene<sup>101,102</sup>, Late  
804 Cretaceous<sup>5</sup> as well as estimates of future climate<sup>100,103</sup>.

805

### 806 **Sr and Nd isotopic measurements**

807 A total of seven samples were selected for processing from cores 9R and 10R at site  
808 PS104\_20-2. A detailed method description that was applied for determining their Sr and Nd  
809 isotopic compositions is given in ref. 104.

810

### 811 **Zircon and apatite U-Pb geochronology**

812 The youngest detrital zircon and apatite U-Pb ages obtained from the cores 2R (sample AWI-  
813 35 at 9.9 mbsf) and 9R (sample AWI-25 at 26.7 mbsf) were used for constraining maximum  
814 deposition ages of the sandstone. The samples yielded Eocene apatite (n=2) and zircon  
815 (n=1) ages. The single Eocene zircon grain yields a Concordia age of 45.5±2.0 Myr  
816 (Extended Data Fig. 1a). The apatite grains all yield analyses discordant in U-Pb isotopic  
817 space due to the presence of common-Pb (Pb<sub>c</sub>; i.e. Pb incorporated during crystallisation as  
818 opposed to radiogenic Pb\* generated *in-situ* by radionuclide decay). For single-grain ages a  
819 terrestrial Pb-isotope evolution model<sup>105</sup> was used for an initial estimate of <sup>207</sup>Pb/<sup>206</sup>Pb<sub>c</sub>,  
820 followed by an iterative approach to the <sup>207</sup>Pb-based corrected age calculation<sup>106</sup>.

821 As only two Eocene single-grain apatite ages are reported, calculation of an array age would  
822 not normally be indicated. However, comparison of the trace element chemistry (REE-Sr-Y)  
823 to an apatite compositional reference library<sup>107</sup> indicates both Eocene grains are chemically  
824 as well as chronologically indistinguishable (Extended Data Fig. 1b), increasing the likelihood



825 of a common source. Therefore, the two youngest apatite grains from AWI-35 were jointly  
826 regressed with the range of  $^{207}\text{Pb}/^{206}\text{Pb}_c$  values ( $0.834 \pm 0.018$ ) for West Antarctic crystalline  
827 basement<sup>108</sup> (Extended Data Fig. 1a) to obtain a lower-intercept age of  $39.3 \pm 3.8$  Myr (MSWD  
828 = 0.99), similar to the independently-obtained single-grain Concordia age of  $45.5 \pm 2.0$  Myr  
829 yielded by the youngest zircon from AWI-25. A Lutetian maximum deposition age (ca. 43  
830 Myr) for AWI-35 and AWI-25 is therefore indicated.

831 Pure apatite and zircon separates were handpicked from the non-magnetic heavy mineral  
832 63-315  $\mu\text{m}$  size fraction, mounted in epoxy resin, ground to reveal internal surfaces, and  
833 polished. Virtually no sample bias was introduced by grain selection because in most cases  
834 all observed mineral grains were picked as the amount of sample material was very small. All  
835 U-Pb analyses were carried out using a Photon Machines Analyte Excite 193 nm ArF  
836 excimer laser-ablation system with a HelEx 2-volume ablation cell coupled to an Agilent 7900  
837 ICPMS at the Department of Geology, Trinity College Dublin, Ireland. Laser fluence was  
838  $2.5 \text{ J cm}^{-2}$  with a repetition rate of 15 Hz and analysis time of 20 s, followed by an 8 s pause  
839 to allow for signal washout and a subsequent baseline measurement. Spot sizes of 47  $\mu\text{m}$   
840 and 24  $\mu\text{m}$  were employed for apatite and zircon respectively, in separate analytical  
841 sessions.

842 Data reduction employed the Vizual\_Age and VisualAge\_UComPbine data reduction  
843 schemes (DRS) for Iolite for zircon and apatite, respectively<sup>109-111</sup>. Each DRS corrects for  
844 intra-session analytical drift, mass bias, and downhole fractionation using a user-specified  
845 fractionation model based on measurements of the primary standard; additionally,  
846 VisualAge\_UComPbine permits the presence of a variable  $\text{Pb}_c$  content in a primary age  
847 standard to be corrected for using a known initial  $^{207}\text{Pb}/^{206}\text{Pb}_c$  value. Final U-Pb age  
848 calculations were made using the Isoplot add-in for Excel<sup>112</sup>.

849 Single-grain zircon U-Pb Concordia ages were calculated, and analyses with probability of  
850 concordance  $< 0.001$  were rejected<sup>112</sup>. The primary standard was Plešovice zircon; the GZ7  
851 and 91,500 zircons were utilised as secondary standards and treated as unknowns during

852 data reduction and age calculation<sup>113</sup>, yielding Concordia ages of 530.1±3.7 Myr and  
853 1060.4±6.8 Myr, respectively.

854 For apatite analyses, Madagascar apatite was employed as the primary standard and  
855 McClure Mountain and Durango apatites were employed as secondary standards<sup>114,115</sup>. Pb<sub>c</sub>  
856 in the secondary standards was corrected for using fixed initial ratios, yielding weighted  
857 mean ages of 532.2±6.0 Myr and 32.3±0.7 Myr, respectively. Variable common Pb contents  
858 in the detrital apatite unknowns were corrected by using a terrestrial Pb evolution model<sup>104</sup>  
859 for calculation of single-grain ages followed by an iterative calculation to obtain single-  
860 analysis <sup>207</sup>Pb-corrected ages<sup>105</sup>. Alternatively, the range of <sup>207</sup>Pb/<sup>206</sup>Pb<sub>c</sub> values for West  
861 Antarctic basement<sup>106</sup> can be used for the single-grain age calculation: the resulting single-  
862 grain ages are within 1 Myr of the single-grain ages obtained using the iterative calculation.  
863 Apatite U-Pb age filtering<sup>116</sup> permitted grains with ages of 10–100 Myr to have 2σ errors  
864 ≤50% and grains with ages >100 Myr to have 2σ errors ≤25%. For apatite trace-element  
865 analysis, the Lolite Trace Elements DRS was utilised. NIST612 glass and Madagascar  
866 apatite<sup>117</sup> were employed as the primary and secondary reference materials respectively,  
867 with <sup>43</sup>Ca as an internal elemental standard<sup>118</sup>.

868

- 869 56. Stalling, D., Westerhoff, M. & Hege, H.-C. Amira: A Highly Interactive System for  
870 Visual Data Analysis. *In: Hansen, C. D. and Johnson, C. R. (eds.) The Visualization*  
871 *Handbook, Elsevier, The Netherlands, 749–767 (2005).*
- 872 57. Raine, J.I., Mildenhall, D.C. & Kennedy, E.M. New Zealand fossil spores and pollen:  
873 an illustrated catalogue. 4th edition. *GNS Science miscellaneous series 4*,  
874 <http://data.gns.cri.nz/sporepollen/index.htm>" (2011).
- 875 58. Mays, C. A late Cretaceous (Cenomanian-Turonian) south polar palynoflora from the  
876 Chatham Islands, New Zealand. *Memoirs of the Association of Australasian*  
877 *Palaeontologists* **47**, 92 pp (2015).
- 878 59. Bowman, V. C., Francis, J. E., Askin, R. A., Riding, J. B. & Swindles, G. T. Latest  
879 Cretaceous-earliest Paleogene vegetation and climate change at the high southern

- 880 latitudes: palynological evidence from Seymour Island, Antarctic Peninsula.  
881 *Palaeogeogr. Palaeoclimatol. Palaeoecol.* **408**, 26–47 (2014).
- 882 60. Utescher, T. et al. The Coexistence Approach—Theoretical background and practical  
883 considerations of using plant fossils for climate quantification. *Palaeogeogr.*  
884 *Palaeoclimatol. Palaeoecol.* **410**, 58–73 (2014).
- 885 61. Ballantyne, A.P., Greenwood, D.R., Sinninghe Damsté, J.S., Csank, A.Z., Eberle, J.J.  
886 & Rybczynski, N. Significantly warmer Arctic surface temperatures during the  
887 Pliocene indicated by multiple independent proxies. *Geology* **38**, 603–606 (2010).
- 888 62. Uhl, D., Mosbrugger, V., Bruch, A. & Utescher, T. Reconstructing palaeotemperatures  
889 using leaf floras-case studies for a comparison of leaf margin analysis and the  
890 coexistence approach. *Rev Palaeobot and Palynol* **126**, 49–64 (2003).
- 891 63. Pound, M.J. & Salzmann, U. Heterogeneity in global vegetation and terrestrial climate  
892 change during the late Eocene to early Oligocene transition. *Scientific Reports* **7**,  
893 43386 (2017).
- 894 64. Pross, J. et al. Persistent near-tropical warmth on the Antarctic continent during the  
895 early Eocene epoch. *Nature* **488**, 73–77 (2012).
- 896 65. Willard, D. A. et al. Arctic vegetation, temperature, and hydrology during Early  
897 Eocene transient global warming events. *Global and Planetary Change* **178**, 139–152  
898 (2019).
- 899 66. Kennedy, E.M. Late Cretaceous and Paleocene terrestrial climates of New Zealand:  
900 leaf fossil evidence from South Island assemblages. *N. Z. J. Geol. Geophys.* **46**, 295–  
901 306 (2003).
- 902 67. Kennedy, E.M., Arens, N.C., Reichgelt, T., Spicer, R.A., Spicer, T.E.V., Stranks, L.,  
903 Yang, J. Deriving temperature estimates from southern hemisphere leaves.  
904 *Palaeogeogr. Palaeoclimatol. Palaeoecol.* **412**, 80–90 (2014).
- 905 68. Grimm, G. W., Bouchal, J. M., Denk, T. & Potts, A. Fables and foibles: A critical  
906 analysis of the Palaeoflora database and the Coexistence Approach for  
907 palaeoclimate reconstruction. *Rev. Palaeobot. Palynol.* **233**, 216–235 (2016).

- 908 69. Hollis, C. J. et al. The DeepMIP contribution to PMIP4: methodologies for selection,  
909 compilation and analysis of latest Paleocene and early Eocene climate proxy data,  
910 incorporating version 0.1 of the DeepMIP database. *Geosci. Model Dev.* **12**, 3149–  
911 3206 (2019).
- 912 70. Kühl, N., Gebhardt, C., Litt, T. & Hense, A. Probability Density Functions as  
913 Botanical-Climatological Transfer Functions for Climate Reconstruction. *Quat. Res.*  
914 **58**, 381–392 (2002).
- 915 71. Greenwood, D.R., Keefe, R.L., Reichgelt, T. & Webb, J.A. Eocene paleobotanical  
916 altimetry of Victoria's Eastern Uplands. *Australian Journal of Earth Sciences* **64**, 625–  
917 637 (2017).
- 918 72. Harbert, R. S. & Nixon, K. C. Climate reconstruction analysis using coexistence  
919 likelihood estimation (CRACLE): A method for the estimation of climate using  
920 vegetation. *American Journal of Botany* **102**, 1277–1289 (2015).
- 921 73. GBIF. The Global Biodiversity Information Facility. What is GBIF?. Available from  
922 <https://www.gbif.org/what-is-gbif> [15.5.2019] (2019).
- 923 74. Fick, S.E. & Hijmans, R.J. WorldClim 2: new 1-km spatial resolution climate surfaces  
924 for global land areas. *Int. Journ. of Climatol.* **37**, 4302–4315 (2017).
- 925 75. Hijmans, R.J, Phillips, S., Leathwick, J. & Elith, J. Package 'dismo'. Available online  
926 at: <http://cran.r-project.org/web/packages/dismo/index.html> (2011).
- 927 76. Reichgelt, T., West, C. K. & Greenwood, D. R. The relation between global palm  
928 distribution and climate. *Scientific Reports* **8**, 4721 (2018).
- 929 77. Bourbonniere, R. A. & Meyers, P. A. Sedimentary geolipid records of historical  
930 changes in the watersheds and productivities of Lakes Ontario and Erie. *Limnology*  
931 *and Oceanography* **41**, 352–359 (1996).
- 932 78. Rütters, H. Sass, H., Cypionka, H. & Rullkötter, J. Phospholipid analysis as a toll to  
933 study complex microbial communities in marine sediments. *J. Microbiol. Meth.* **48**,  
934 149–160 (2002).

- 935 79. Bauersachs, T., Talbot, H. M., Sidgwick, F., Sivonen, K. & Schwark, L. Lipid  
936 biomarker signatures as tracers for harmful cyanobacterial blooms in the Baltic Sea.  
937 *PLOS ONE* **12**, doi:10.1371/journal.pone.0186360 (2017).
- 938 80. Bauersachs, T., et al. Rapid analysis of long-chain glycolipids in heterocystous  
939 cyanobacteria using high-performance liquid chromatography coupled to electrospray  
940 ionization tandem mass spectrometry. *Rapid Comm. in Mass Spectrometry* **23**, 1387–  
941 1394 (2009).
- 942 81. Bauersachs, T., et al. Distribution of long chain heterocyst glycolipids in cultures of  
943 the thermophilic cyanobacterium *Mastigocladus laminosus* and a hot spring microbial  
944 mat. *Org. Geochem.* **56**, 19 – 24 (2013).
- 945 82. Wörmer, L., et al. Cyanobacterial heterocyst glycolipids in cultures and environmental  
946 samples: Diversity and biomarker potential. *Limnol. Oceanogr.* **57**, 1775–1788  
947 (2012).
- 948 83. Schouten, S., et al. Endosymbiotic heterocystous cyanobacteria synthesize different  
949 heterocyst glycolipids than free-living heterocyst cyanobacteria. *Phytochemistry* **85**,  
950 115–121 (2013).
- 951 84. Bale, N. J., et al. A novel heterocyst glycolipid detected in a pelagic N<sub>2</sub>-fixing  
952 cyanobacterium of the genus *Calothrix*. *Org. Geochem.* **123**, 44–47 (2018).
- 953 85. Bauersachs, T., Miller, S. R., Gugger, M., Mudimu, O., Friedl, T. & Schwark, L.  
954 Heterocyte glycolipids indicate polyphyly of stigonematalean cyanobacteria.  
955 *Phytochem.* **166**, doi:10.1016/j.phytochem.2019.112059 (2019).
- 956 86. Ehrmann, W. et al. Provenance changes between recent and glacial-time sediments  
957 in the Amundsen Sea Embayment, West Antarctica: clay mineral assemblage  
958 evidence. *Antarctic Science* **23**, 471–486 (2011).
- 959 87. Petschick, R., Kuhn, G. & Gingele, F. Clay mineral distribution in surface sediments  
960 of the South Atlantic: sources, transport, and relation to oceanography. *Mar. Geol.*  
961 **130**, 203–229 (1996).

- 962 88. Kirschvink, J. L. The least-squares line and plane and the analysis of paleomagnetic  
963 data. *J. Royal Astr. Soc.* **62**, 699–718 (1980).
- 964 89. Roeckner, E., et al. The atmospheric general circulation model ECHAM 5. In: PARTI:  
965 Model Description, Report 349, Max-Planck-Institut für Meteorologie, Hamburg  
966 (2003).
- 967 90. Marsland, S.J., Haak, H., Jungclaus, J.H., Latif, M. & Roske, F. The Max-Planck-  
968 Institute global ocean/sea ice model with orthogonal curvilinear coordinates. *Ocean*  
969 *Model* **5**, 91–127 (2003).
- 970 91. Hagemann, S. & Dumenil, L. A parametrization of the lateral waterflow for the global  
971 scale. *Clim. Dyn.* **14**, 17–31 (1997).
- 972 92. Hibler III, W.D. A dynamic thermodynamic sea ice model. *J. Phys. Oceanogr.* **9**, 815–  
973 846 (1979).
- 974 93. Markwick, P.J. & Valdes, P.J. Palaeo-digital elevation models for use as boundary  
975 conditions in coupled ocean–atmosphere GCM experiments: a Maastrichtian (late  
976 Cretaceous) example. *Palaeogeogr. Palaeoclimatol. Palaeoecol.* **213**, 37–63 (2004).
- 977 94. Sewall, J.O., Van de Wal, R.S.W., Van Der Zwan, K., Van Oosterhout, C., Dijkstra,  
978 H.A. & Scotese, C.R. Climate model boundary conditions for four Cretaceous time  
979 slices. *Clim. Past* **3**, 647–657 (2007).
- 980 95. Niezgodzki, I., Tyszka, J., Knorr, G., & Lohmann, G. Was the Arctic Ocean ice free  
981 during the latest Cretaceous? The role of CO<sub>2</sub> and gateway configurations. *Global*  
982 *and Planetary Change* **177**, 201–212 (2019).
- 983 96. Wei, W. & Lohmann, G. Simulated Atlantic Multidecadal Oscillation during the  
984 Holocene. *J. Climate* **25**, 6989–7002 (2012).
- 985 97. Zhang, X., Lohmann, G., Knorr, G., & Purcell, C. Abrupt glacial climate shifts  
986 controlled by ice sheet changes. *Nature* **512**, 290–294 (2014).
- 987 98. Stepanek, C. & Lohmann, G. Modelling mid-Pliocene climate with COSMOS.  
988 *Geosci. Model Dev.* **5**, 1221–1243 (2012).

- 989 99. Knorr, G. & Lohmann, G. Climate warming during Antarctic ice sheet expansion at  
990 the Middle Miocene transition. *Nat. Geosci.* **7**, 376–381 (2014).
- 991 100. Stein, R. *et al.* Evidence for ice-free summers in the late Miocene central  
992 Arctic Ocean. *Nat. Comm.* **7**, 11148 (2016).
- 993 101. Walliser, E.O., Lohmann, G., Niezgodzki, I., Tütken, T. & Schöne, B.R.  
994 Response of Central European SST to atmospheric pCO<sub>2</sub> forcing during the  
995 Oligocene – A combined proxy data and numerical climate model approach.  
996 *Palaeogeogr. Palaeoclimatol. Palaeoecol.* **459**, 552–569 (2016).
- 997 102. Vahlenkamp, M., *et al.* Astronomically Paced Changes in Deep-Water  
998 Circulation in the Western North Atlantic during the Middle Eocene. *Earth Planet. Sci.*  
999 *Lett.* **484**, 329–340 (2018).
- 1000 103. Gierz, P., Lohmann, G. & Wei, W. Response of Atlantic Overturning to Future  
1001 Warming in a coupled Atmosphere-Ocean-Ice Sheet Model. *Geophys. Res. Lett.* **42**,  
1002 6811–6818 (2015).
- 1003 104. Simões Pereira, P., van de Flierdt, T., Hemming, S.R., Hammond, S.J., Kuhn,  
1004 G., Brachfeld, S., Doherty, C. & Hillenbrand, C.D. Geochemical fingerprints of  
1005 glacially eroded bedrock from West Antarctica: Detrital thermochronology, radiogenic  
1006 isotope systematics and trace element geochemistry in Late Holocene glacial-marine  
1007 sediments. *Earth-Science Rev.* **182**, 204-232 (2018).
- 1008 105. Stacey, J. S. & Kramers, J.D. Approximation of terrestrial lead isotope  
1009 evolution by a two-stage model. *Earth Planet. Sci. Lett.* **26**, 207–221 (1975).
- 1010 106. Chew, D. M., Sylvester, P. J. & Tubrett, M. N. U–Pb and Th–Pb dating of  
1011 apatite by LA-ICPMS. *Chem. Geol.* **280**, 200–216 (2011).
- 1012 107. O’Sullivan, G. J., Chew, D. M., Morton, A. C., Mark, C. & Henrichs, I. A. An  
1013 Integrated Apatite Geochronology and Geochemistry Tool for Sedimentary  
1014 Provenance Analysis. *Geochem. Geophys. Geosys.* **19**, 1309–1326 (2018).
- 1015 108. Flowerdew, M.J., Tyrrell, S., Riley, T.R., Whitehouse, M.J., Mulvaney, R.,  
1016 Leat, P.T. & Marschall, H.R. Distinguishing East and West Antarctic sediment sources

- 1017 using the Pb isotope composition of detrital K-feldspar. *Chem. Geol.* **292–293**, 88–  
1018 102 (2012).
- 1019 109. Petrus, J. A., & Kamber, B. S. VizualAge: A novel approach to laser ablation  
1020 ICP MS U Pb geochronology data reduction. *Geostandards and Geoanalytical*  
1021 *Research* **36**, 247–270 (2012).
- 1022 110. Chew, D.M., Petrus, J. A. & Kamber, B. S. U-Pb LA-ICPMS dating using  
1023 accessory mineral standards with variable common Pb. *Chem. Geol.* **363**, 185–199  
1024 (2014).
- 1025 111. C. Paton, Hellstrom, J., Paul, B.; Woodhead, J., Hergt, J. Lolite: freeware for  
1026 the visualisation and processing of mass spectrometric data. *J. Anal. At.*  
1027 *Spectrom.* **26**, 2508–2518 (2011).
- 1028 112. Ludwig, K. R. User's manual for Isoplot 3.75: A geochronological Toolkit for  
1029 Microsoft Excel. *Berkeley Geochronology Center Special Publication* **4**, 70 (2012).
- 1030 113. Nasdala, L. et al. GZ7 and GZ8 - Two Zircon Reference Materials for SIMS U-  
1031 Pb Geochronology. *Geostandards and Geoanalytical Research* **42**, 431–457 (2018).
- 1032 114. McDowell, F. W., McIntosh, W. C. & Farley, K. A. A precise  $^{40}\text{Ar}$ – $^{39}\text{Ar}$   
1033 reference age for the Durango apatite (U–Th)/He and fission-track dating standard.  
1034 *Chem. Geol.* **214**, 249–263 (2005).
- 1035 115. Schoene, B. & Bowring, S. A. U–Pb systematics of the McClure Mountain  
1036 syenite: thermochronological constraints on the age of the  $^{40}\text{Ar}/^{39}\text{Ar}$  standard  
1037 MMhb. *Contributions to Mineralogy and Petrology* **151**, 615 (2006).
- 1038 116. Mark, C., Cogné, N. & Chew, D. Tracking exhumation and drainage divide  
1039 migration of the western Alps: a test of the apatite U-Pb thermochronometer as a  
1040 detrital provenance tool. *GSA Bulletin* **128**, 1439–1460 (2016).
- 1041 117. Mao, M., Rukhlov, A.S., Rowins, S.M., Spence, J. & Coogan, L.A. Apatite  
1042 trace element compositions: A robust new tool for mineral exploration. *Econom. Geol.*  
1043 **111**, 1187–1222 (2016).



1044 118. Woodhead, J.D., Hellstrom, J., Hergt, J.M., Greig, A. & Maas, R. Isotopic and  
1045 elemental imaging of geological materials by laser ablation inductively coupled  
1046 plasma-mass spectrometry. *Geostandards and Geoanalytical Research* **31**, 331–343  
1047 (2007).

1048

1049

1050 **Data availability**

1051 All data are available online in the *Data Base for Earth and Environmental Science*

1052 (PANGAEA) (DOI registration in progress). The dataset can be accessed via

1053 <https://doi.pangaea.de/10.1594/PANGAEA.906092>.

1054

1055 **Code availability**

1056 The standard model code of the ‘Community Earth System Models’ (COSMOS) version

1057 COSMOS-landveg r2413 (2009) is available upon request from the ‘Max Planck Institute for

1058 Meteorology’ in Hamburg (<https://www.mpimet.mpg.de>). Analytical scripts are available in the

1059 PANGAEA database (<https://doi.pangaea.de/10.1594/PANGAEA.910179>).

1060

1061 Extended Data Figure 1: Tera-Wasserburg and PCA plots for uranium/lead (U/Pb) ages (in

1062  $\pm$ Myr). a) Tera-Wasserburg diagram showing apatite (red; 9.9 mbsf) and zircon (blue; 26.7

1063 mbsf) U-Pb data. Red bar at upper array intercept for Eocene apatite is the range of

1064 crystalline basement  $^{207}\text{Pb}_c/^{206}\text{Pb}_c$  values reported by (ref. 105) for West Antarctica, which

1065 anchor the apatite age calculation. Data-point error ellipses are  $2\sigma$ . b) PCA plot showing

1066 trace-element data and single-grain ages for AWI-35 (9.9 mbsf) apatite, and lithological fields

1067 derived from bedrock apatite reference library<sup>105</sup>. Eocene grains (labelled in red) are

1068 chemically as well as chronologically distinct from other detrital apatite in the same sample.

1069 Data-point error ellipses are  $2\sigma$ .

1070

1071 Extended Data Figure 2: Pollen abundance diagram. Percentages of most abundant pollen  
1072 and spores and their total counts in cores 9R and 10R at site PS104\_20-2.

1073

1074 Extended Data Figure 3: Photomicrographs of selected pollen and spores. a. *Cyathidites*  
1075 *australis*; b. *Osmundacidites wellmanii*; c. *Ruffordiaspora australiensis*; d. *Ruffordiaspora*  
1076 *ludbrookiae*; e. *Cycadopites follicularis*; f. *Microcachrydites antarcticus*; g. *Phyllocladidites*  
1077 *mawsonii*; h. *Podocarpidites major*; i. *Trichotomosulcites hemisphaerius*; j.  
1078 *Trichotomosulcites subgranulatus*; k. *Taxodiaceapollenites hiatus*; l. *Equisetosporites sp.*;  
1079 m. *Nyssapollenites chathamicus*; n. *Peninsulapollis gillii*; o. *Proteacidites subpalisadus*. All  
1080 scale bars: 10  $\mu$ m.

1081

1082 Extended Data Figure 4: Heterocyst glycolipid (HG) palaeothermometry. Presence of  
1083 heterocyst glycolipids at 27.03–27.04 mbsf at site PS104\_20-2 (core 9R) and river or lake  
1084 surface water temperature (SWT) estimates from the heterocyst glycolipid-based molecular  
1085 palaeothermometer.

1086

1087 Extended Data Figure 5: Example of microscopic images from thin sections. The sections  
1088 are taken from a fossil root fragment between 29.34 and 29.43 mbsf in core 10R at site  
1089 PS104\_20-2. a) Overview scan of root fragment with indicated locations of detailed  
1090 microscopic images b–e. White arrows indicate locations of preserved parenchyma storage  
1091 cells including potential aerenchyma gas exchange cells (d). The scale bar in “d” applies to  
1092 figures b–e.

1093

1094 Extended Data Figure 6: Biomarker presence. a) Pristane/*n*-C<sub>17</sub> versus phytane/*n*-C<sub>18</sub> to infer  
1095 organic matter type during sediment deposition (after refs. 39, 40). b) Carbon preference  
1096 index (CPI) and pristane/phytane (Pr/Ph) ratios. The CPI points to a low maturity and land  
1097 plant origin of the organic matter (CPI > 1) deposited in an aquatic environment (Pr/Ph <2)  
1098 and a peat swamp environment (Pr/Ph >2), respectively.

1099

1100 Extended Data Table 1: Percentages of most abundant pollen and spore taxa.

1101

1102 Extended Data Table 2: Selected key pollen taxa and NLR used to derive quantitative

1103 climate estimates.

1104

1105 Extended Data Table 3: Full list of identified pollen and spore taxa. All taxa identified during

1106 the current study are included. Question marks show uncertain taxa identifications, which

1107 require further studies. Those taxa marked with an asterisk have also been described from

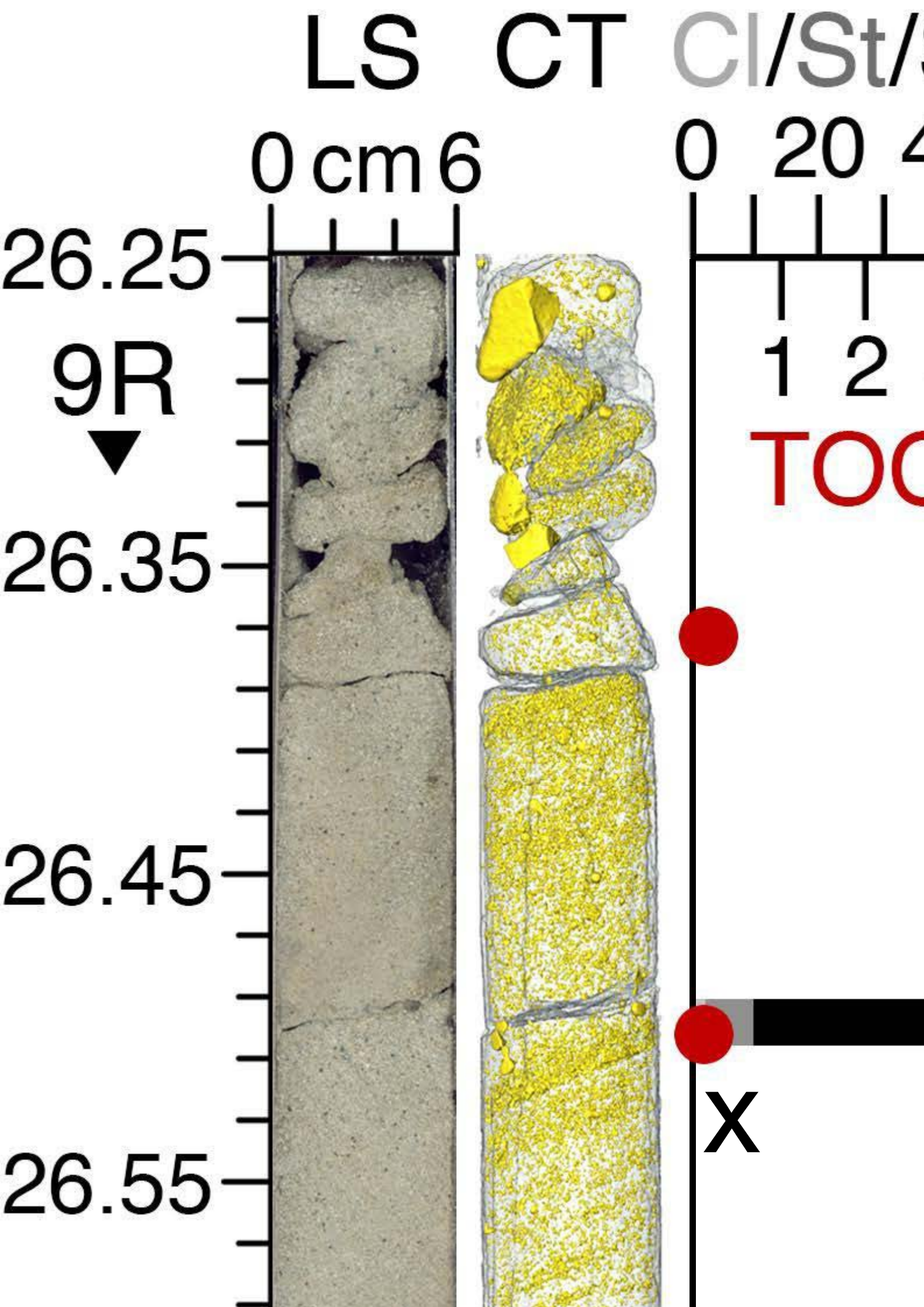
1108 the Tupuangi Formation on the Chatham Islands<sup>30,58</sup>.

a)



South Pole  
+

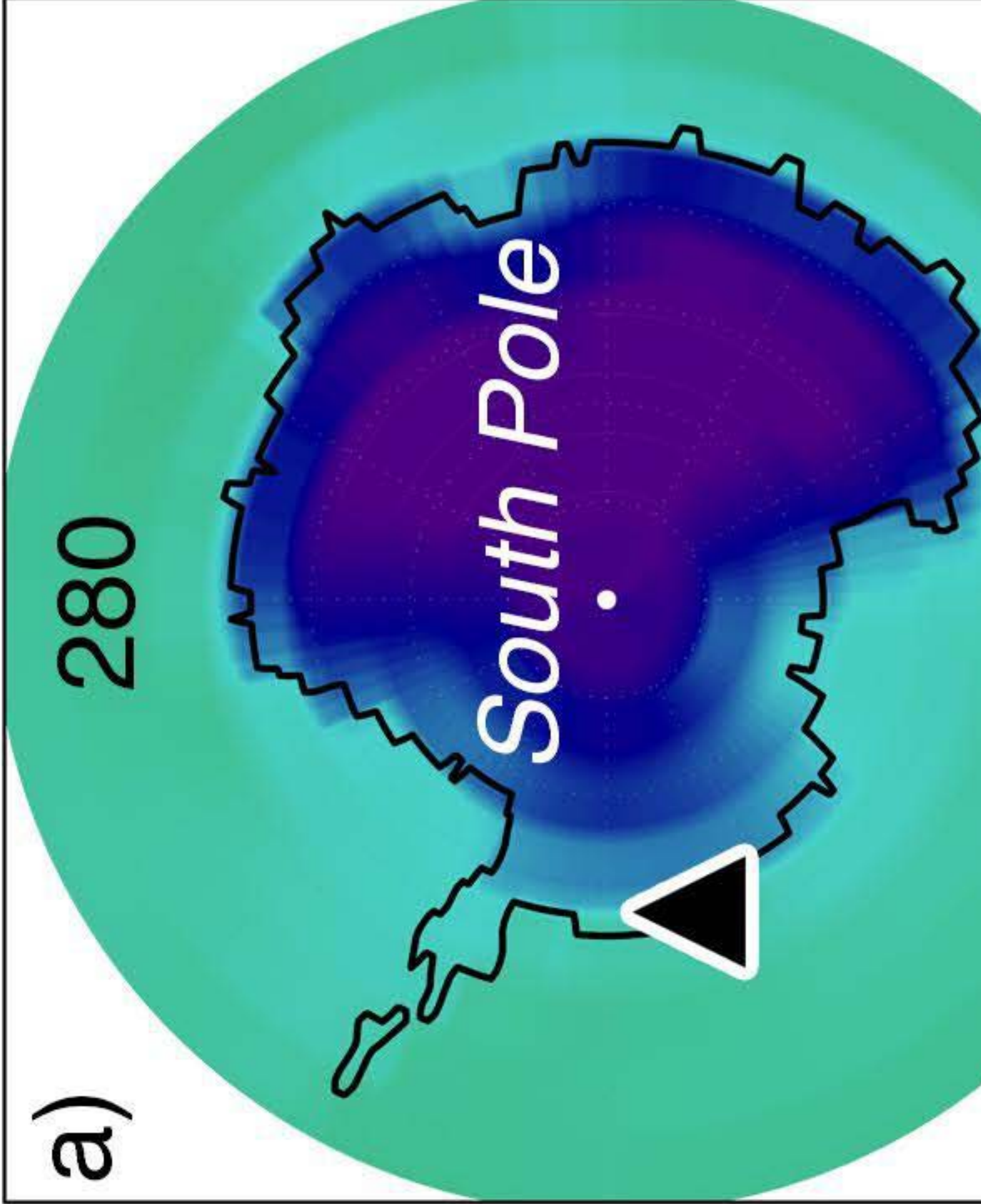
Antarctica



a)

280

South Pole



b)

